Publications of the Astronomical Society of the Pacific, 138:094202 (30pp), 2026 September https://doi.org/10.1088/1538-3873/ae9c97
© 2026. The Author(s). Published by IOP Publishing Ltd on behalf of the Astronomical Society of the Pacific (ASP).

OPEN ACCESS

CPD–82 291: Multi-sector TESS Photometry and SED Analysis of an Active Eclipsing Binary

Volkan Bakış and Gökhan Yücel
Department of Space Sciences and Technologies, Faculty of Science, Akdeniz University, 07058, Antalya, Türkiye; volkanbakis@akdeniz.edu.tr
Received 2026 May 20; revised 2026 August 18; accepted 2026 August 20; published 2026 September 8

Abstract

We present a multi-sector TESS photometric and spectral energy distribution analysis of the eclipsing binary CPD–82 291 (RX J0853.1–8244). Eight TESS sectors reveal well-defined eclipses and substantial, changing out-of-eclipse modulation. The asymmetries are reproduced by different surface-brightness configurations at different epochs, consistent with strong and evolving stellar activity, although the fitted circular regions are not unique maps of individual starspots. A detached-binary light-curve model yields an orbital inclination of $i \simeq 82.^{\circ}1$ and a photometric mass ratio of $q_{\rm phot} \simeq 0.464$. Without a spectroscopic radial-velocity orbit, the mass ratio and absolute parameters are model dependent rather than dynamical measurements. Combining the light-curve geometry with the SED radius scale and *Gaia* distance gives $R_1 \simeq 1.25\,R_{\odot}$ and $R_2 \simeq 3.70\,R_{\odot}$; the corresponding model-inferred masses remain substantially less secure than the dimensionless light-curve parameters. The stellar photospheres reproduce the observed SED from the optical region through WISE W4, with no statistically significant mid-infrared excess. The only positive long-wavelength deviation is a low-significance 60 μm measurement, while the 90 μm result is an upper limit. A cool circumbinary-dust model can reproduce this tentative signal, but such a component is not required by the photometry, and its inferred mass and radial extent are non-unique and strongly model dependent. Evolutionary tracks place the primary close to the zero-age main sequence and the secondary well above the main-sequence locus. However, the absence of radial velocities and spectroscopic youth indicators, together with Gaia astrometry inconsistent with Chamaeleon I membership, prevents a secure pre-main-sequence classification. CPD–82 291 is therefore best regarded as an active eclipsing binary with uncertain evolutionary status and only a marginal far-infrared indication that could be reproduced by cool circumstellar material.

Unified Astronomy Thesaurus concepts: Eclipsing binary stars (444); Pre-main sequence stars (1290); Young stellar objects (1834); Protoplanetary disks (1300); Spectral energy distribution (2129)

1. Introduction

Mass and radius are the fundamental parameters governing stellar structure and evolution, and their accurate determination across a wide range of masses and ages is essential for constraining theoretical models. Detached eclipsing binaries with well-sampled eclipse light curves and double-lined spectroscopic radial-velocity measurements provide the most direct and reliable measurements of these quantities, because they enable largely model-independent determinations of the stellar masses, radii, and orbital scale (Torres et al. 2010; Serenelli et al. 2021). For this reason, eclipsing systems serve as critical benchmarks for testing stellar-evolution theory. In the absence of a spectroscopic orbit, however, the light curve primarily constrains the orbital geometry, fractional radii, temperature ratio, and, under favourable conditions, a model-dependent photometric mass ratio. The absolute masses and orbital scale must then be inferred using additional assumptions or external constraints and are therefore not direct dynamical measurements.

Young eclipsing binaries are particularly valuable laboratories for testing stellar evolutionary models, since they probe the pre-main-sequence (PMS) phase during which stellar properties such as radius, luminosity, and effective temperature evolve rapidly. Fundamental parameters derived from eclipsing binaries with both photometric and spectroscopic orbital solutions provide some of the most stringent observational constraints on PMS evolution, especially in the low- and intermediate-mass regime where theoretical models still show significant uncertainties (e.g. Stassun et al. 2014; Gillen et al. 2017).

Despite substantial observational progress in recent years, important discrepancies between theoretical predictions and observed stellar properties remain. In particular, many PMS systems exhibit inflated stellar radii, lower effective temperatures, and luminosities that are difficult to reproduce

Original content from this work may be used under the terms of the Creative Commons Attribution 4.0 licence. Any further distribution of this work must maintain attribution to the author(s) and the title of the work, journal citation and DOI.

simultaneously with standard evolutionary models. These discrepancies are often attributed to magnetic activity, starspots, accretion history, or remaining limitations in PMS evolutionary calculations for young low-mass stars (e.g. Stassun et al. 2014; Gillen et al. 2017).

The number of known PMS eclipsing binaries has increased considerably over the last decade thanks to wide-field photometric surveys and space-based missions. Recent discoveries include systems such as MML 48 (Chew & Hebb 2025), Mon–735 (Gillen et al. 2020), THOR–42 (Murphy et al. 2020), TOI–450 (Tofflemire et al. 2023), and several newly identified PMS eclipsing binaries summarized by Chew & Hebb (2025). Nevertheless, the currently known sample remains relatively limited and does not yet fully cover the parameter space required for robust calibration of PMS evolutionary models, particularly for active low-mass systems, inflated secondaries, and binaries associated with circumstellar or circumbinary material. The value of individual systems as evolutionary benchmarks nevertheless depends strongly on the availability of spectroscopic orbital constraints and on the security of their youth and association membership.

In addition to analyses based on light curves and radial velocities, the spectral energy distribution (SED) provides an independent and complementary diagnostic of stellar systems. In young stellar objects (YSOs), circumstellar material such as discs and envelopes can contribute significantly to the observed flux, particularly at infrared wavelengths, and can also introduce additional extinction components. As a result, extinction estimates derived from large-scale Galactic reddening maps may not accurately represent the true line-of-sight attenuation toward individual systems. SED modelling can therefore provide useful constraints on stellar radii, extinction, and infrared-excess components, although the inferred circumstellar properties remain dependent on the adopted geometry, opacity prescription, distance, and treatment of non-simultaneous photometry.

CPD–82 291 (RX J0853.1–8244; ASASSN-V J085305.34–824360.0) was originally classified as a weak-line T Tauri star in the direction of the Chamaeleon I star-forming region (Spangler et al. 2001). However, its youth and association membership have not been established unambiguously. In the Spitzer Formation and Evolution of Planetary Systems survey, Carpenter et al. (2009) classified the source as a field star with an activity-based age estimate of $\log(\mathrm{age/yr}) = 8.6$. They found its 16–8 and 24–8 μm flux ratios to be consistent with photospheric emission and reported no significant infrared excess in the IRAC, IRS, MIPS 24 μm, or MIPS 70 μm observations. The absence of a significant excess in the Spitzer and WISE mid-infrared measurements, together with the low-significance 60 μm flux reported by Spangler et al. (2001), indicates that the available photometry does not establish a persistent infrared excess. The far-infrared emission is therefore treated in this study as tentative and is explored only through a conditional dust model.

The Gaia DR3 astrometry does not support physical membership in Chamaeleon I. CPD–82 291 has proper-motion components of $\mu_{\alpha*} = +3.435 \pm 0.0169$ and $\mu_\delta = -13.006 \pm 0.014$ mas yr^{-1}, whereas the northern and southern Chamaeleon I subclusters have mean proper motions of approximately $(-22.07, -0.05)$ and $(-23.13, +1.59)$ mas yr^{-1}, respectively (Roccatagliata et al. 2018). The proper-motion vector of CPD–82 291 is therefore separated from those of the two subclusters by approximately 29–30 mas yr^{-1}. In addition, its corrected parallax, $\varpi_{\mathrm{corr}} = 2.0538 \pm 0.0134$ mas, is markedly smaller than the mean Chamaeleon I parallax of approximately 5.25 mas. The source is thus located roughly 300 pc farther away along the line of sight than the association. Its Gaia DR3 RUWE value of 0.885 does not indicate a poor astrometric fit. We therefore conclude that CPD–82 291 is not a physical member of Chamaeleon I, although its evolutionary status and possible youth must be assessed independently from spectroscopic and stellar-parameter diagnostics.

The eclipsing-binary nature of CPD–82 291 was previously recognized by Christy et al. (2022) in their study of unusual variables identified through the Citizen ASAS-SN project. Using ASAS-SN photometry, they revised the initially reported period of approximately 20.4 days to $P \simeq 10.21$ days and showed that the phase-folded light curve contains both primary and secondary eclipses. They also attributed the prominent sinusoidal modulation to surface activity and starspots in a nearly synchronized binary. Their treatment was primarily classificatory, however, and did not include detailed eclipse modelling or a physical analysis of the stellar and infrared-emitting components.

In the present study, we extend this earlier identification through the analysis of eight sectors of high-precision TESS photometry. We examine the changing out-of-eclipse morphology on a sector-by-sector basis, model the eclipse geometry and evolving surface-brightness distribution, and search for candidate flare events. We further combine the light-curve constraints with broadband photometry and the adopted Gaia distance to investigate the stellar scale and the possible origin of the tentative far-infrared emission. Because no spectroscopic radial-velocity orbit or spatially resolved infrared observation is available, the resulting component masses, orbital scale, and dust-structure parameters are treated as model-inferred quantities rather than as direct dynamical or spatial measurements.

Our principal aim is therefore not to report the discovery of the binary, but to provide a detailed multi-sector photometric characterization of its eclipse morphology and activity, together with a model-dependent investigation of its stellar properties and infrared-emitting environment. The tentative far-infrared emission is explored using a conditional circumbinary-dust model, while alternative explanations such as

Table 1
Photometric Data Adopted for the SED Analysis of CPD–82 291 After Quality-independent Catalogue Matching, Removal of Exact Duplicate Entries, and Combination of Distinct Photometric Records within Each Bandpass

No.	$\lambda_{\rm eff}$ (μm)	Flux (Jy)	Unc. (Jy)	Bandpass	N	Sources	Epoch (JD−2400000)	Err.	Treatment
1	0.3498	0.005288	0.000100	SkyMapper u	5	S1,S2,S3	⋯	C	Excluded
2	0.3519	0.015200	0.000200	SDSS u	1	S4	⋯	C	Excluded
3	0.3871	0.015400	0.000100	SkyMapper v	3	S1,S2,S3	⋯	C	Excluded
4	0.4203	0.033292	0.007039	Tycho B_T	2	S5,S6	⋯	C	Fit
5	0.4442	0.042599	0.003901	Johnson B	6	S7,S8,S9,S10,S11,S12	58072.819	C+I	Fit
6	0.4820	0.060000	0.007700	SDSS g	1	S4	⋯	C	Fit
7	0.4820	0.059900	0.007700	SDSS g'	1	S9	⋯	C	Fit
8	0.4968	0.076350	0.001906	SkyMapper g	4	S1,S2,S3	⋯	C	Fit
9	0.5036	0.071700	0.000600	Gaia DR3 $G_{\rm BP}$	1	S13	⋯	C	Fit
10	0.5046	0.070600	0.000300	Gaia DR2 $G_{\rm BP}$	1	S14	⋯	C	Fit
11	0.5319	0.087456	0.007114	Tycho V_T	3	S5,S6,S15	⋯	C	Fit
12	0.5537	0.086869	0.010102	Johnson V	8	S8,S9,S16,S10,S17,S18, S11,S12	58072.819	C+I	Fit
13	0.5822	0.102000	0.010200	Gaia DR3 G	1	S13	⋯	C+I	Fit
14	0.6003	0.084700	0.008470	IA598	1	S12	⋯	C+I	Fit
15	0.6041	0.098138	0.000644	SkyMapper r	5	S1,S2,S3	⋯	C	Fit
16	0.6226	0.105000	0.010500	Gaia DR2 G	1	S14	⋯	C+I	Fit
17	0.6247	0.089200	0.035600	SDSS r	1	S4	⋯	C	Fit
18	0.6247	0.088900	0.035500	SDSS r'	1	S9	⋯	C	Fit
19	0.6730	0.095621	0.000274	Gaia G (compiled)	4	S19,S16,S20,S21	58072.819	C+I	Fit
20	0.7621	0.147000	0.001000	Gaia DR3 $G_{\rm RP}$	1	S13	⋯	C	Fit
21	0.7635	0.118000	0.042000	SDSS i'	1	S9	⋯	C	Fit
22	0.7635	0.119000	0.042000	SDSS i	1	S4	⋯	C	Fit
23	0.7725	0.150000	0.001000	Gaia DR2 $G_{\rm RP}$	1	S14	⋯	C	Fit
24	0.7886	0.148970	0.008992	Cousins I	20	S22	⋯	C	Fit
25	0.9018	0.166000	0.003000	SDSS z	1	S4	⋯	C	Fit
26	1.2390	0.199500	0.003571	2MASS J	2	S23,S16	58072.819	C	Fit
27	1.2500	0.202638	0.012049	Johnson J	27	S22,S24,S15	51541.725	C	Fit
28	1.6300	0.214872	0.003827	Johnson H	3	S24,S6,S15	51541.725	C	Excluded
29	1.6495	0.216000	0.005000	2MASS H	1	S25	58072.819	C	Excluded
30	2.1638	0.163000	0.003000	2MASS K_s	1	S26	58072.819	C	Excluded
31	2.1900	0.160396	0.008703	Johnson K	22	S22,S24	51541.725	C	Excluded
32	3.3500	0.078420	0.000933	WISE W1	6	S27,S28,S29,S30,S10,S12	57165.259–58072.819	C+I	Fit
33	3.4000	0.073800	0.001600	Johnson L	1	S6	⋯	C	Fit
34	4.6000	0.043730	0.000465	WISE W2	5	S4,S27,S29,S30,S12	57165.259–58072.819	C+I	Fit
35	5.0300	0.040600	0.000700	Johnson M	1	S6	⋯	C	Fit
36	11.5598	0.008055	0.000276	WISE W3	3	S4,S27,S12	58072.819	C+I	Fit
37	22.0907	0.002218	0.000795	WISE W4	2	S27,S31	58072.819	C	Diagnostic
38	60.0005	0.026000	0.019000	60 μm	1	S32	⋯	C	Low-S/N dust constraint
39	90.0000	< 0.021	0.007000	90 μm	1	S32	⋯	C	3σ UL

Notes. Flux densities and their adopted photometric uncertainties are given in Jy. The column N gives the number of distinct photometric records contributing to the tabulated flux after exact duplicate removal. Source codes identify the VizieR catalogue tables contributing to each combined point and are defined below. Epochs are the JD (TCB) values supplied by the VizieR SED service, expressed as JD−2400000; a range is given when more than one finite epoch is available, while "–" indicates that no epoch was supplied. The uncertainty code C denotes points based exclusively on available catalogue uncertainties, whereas C+I denotes combined points for which at least one contributing record lacked a valid catalogue uncertainty and was assigned the wavelength-dependent uncertainty described in Section 3.3. The listed uncertainties do not include the additional 20% systematic term added in quadrature in the SED likelihood. Measurements at $\lambda < 0.4$ μm and $1.5 < \lambda < 3.0$ μm were excluded from the fit. The 60 μm measurement is retained only as a low-significance ($\simeq 1.4\sigma$) flux measurement. The 90 μm entry from Spangler et al. (2001) is a non-detection with a reported 1σ uncertainty of 0.007 Jy and was incorporated as a one-sided 3σ upper limit of 0.021 Jy.

Source identifiers: S1=II/358/smss; S2=II/379/smssdr4; S3=J/ApJ/925/164/catalog; S4=I/353/gsc242; S5=I/350/tyc2tdsc; S6=II/346/jsdc_v2; S7=I/305/out; S8=I/320/spm4; S9=II/336/apass9; S10=IV/38/tic; S11=J/MNRAS/463/4210/ucac4rpm; S12=J/MNRAS/471/770/table1; S13=I/350/gaiaedr3; S14=I/345/gaia2; S15=J/PASP/120/1128/catalog; S16=II/366/catv2021; S17=J/A+A/653/A98/aspic1_1; S18=J/ApJS/203/32/table4; S19=I/339/hsoy; S20=J/A+A/664/A105/main; S21=J/ApJ/867/105/refcat2; S22=B/denis/denis; S23=I/280B/ascc; S24=II/246/out; S25=I/319/xpm; S26=I/317/sample; S27=II/311/wise; S28=II/328/allwise; S29=II/365/catwise; S30=II/369/vexassm; S31=IV/39/tic82; S32=J/ApJ/555/932/targets.

The source identifiers refer to the catalogue tables associated with the distinct photometric records retained after duplicate removal. The complete VizieR provenance, including catalogue entries carrying duplicate copies of the same photometric measurement, was retained during the cleaning procedure but is not reproduced here. Catalogue-specific native quality flags are not propagated as a common field by the homogenized VizieR SED response and therefore are not represented by a single generic quality column in this table.

unresolved contamination, non-simultaneous variability, and different circumstellar geometries are considered when assessing this interpretation.

The structure of the paper is as follows. In Section 2, we describe the observational data and the procedures used to compile and prepare them. Section 3 presents the eclipse-timing, light-curve, SED, surface-brightness, and flare analyses. In Section 4, we present and discuss the binary configuration and model-inferred absolute parameters, the possible evolutionary status of the system, the conditional interpretation of the tentative far-infrared emission, the surface and flare activity, and the principal model limitations. Section 5 summarizes the main conclusions.

2. Observations and Data Preperation

2.1. Broadband Data

Spangler et al. (2001) observed CPD–82 291 using the ISOPHOT C100 detector (Lemke et al. 1996) onboard the Infrared Space Observatory (ISO), employing the 60 μm and 90 μm filters. They reported a flux density of 0.026 ± 0.019 Jy at 60 μm, corresponding to a significance of only approximately 1.4σ. We therefore regard this value as a marginal measurement rather than a secure far-infrared detection. The 90 μm measurement was reported as an upper limit, which is listed explicitly in Table 1 and treated as a one-sided constraint in the SED analysis.

CPD–82 291 was subsequently observed as part of the Spitzer Formation and Evolution of Planetary Systems (FEPS) survey. Carpenter et al. (2009) reported normalized flux ratios of $R_{16/8} = 0.97 \pm 0.05$ and $R_{24/8} = 1.01 \pm 0.03$, both of which are consistent with photospheric emission. They found no significant infrared excess in the IRAC, IRS, MIPS 24 μm, or MIPS 70 μm observations. Thus, the Spitzer measurements do not indicate a persistent mid- or far-infrared excess at the epoch of the FEPS observations.

In addition to the far-infrared measurements reported by Spangler et al. (2001) and the Spitzer/FEPS observations presented by Carpenter et al. (2009), we compiled multi-wavelength photometric data from several surveys using the VizieR photometric data service (Ochsenbein et al. 2000). The SED data were retrieved in flux density units, as provided by the VizieR SED tool, which homogenizes measurements from different photometric systems using appropriate zero-point calibrations. However, the original catalog entries were independently checked to verify the source identifiers, coordinates, angular separations, reported uncertainties, and available photometric quality flags.

The dataset includes optical, near-infrared, and mid-infrared measurements from surveys such as Gaia, 2MASS, and WISE, together with the available ISO and Spitzer measurements and constraints. Catalog entries with uncertain source associations, unreliable quality flags, or possible contamination were excluded from the modelling.

Because CPD–82 291 is photometrically variable and the observations were obtained at different epochs, measurements from different surveys or observing epochs were not averaged into a single representative flux. Instead, individual measurements were retained separately whenever their observing epochs or instrumental characteristics differed. This is particularly important for the infrared data, since the Spitzer and WISE observations exhibit different SED profiles and may sample different states of the unresolved infrared-emitting environment.

The broader point-spread function of WISE, especially in the W3 and W4 bands, also makes its measurements more susceptible to contamination by nearby sources or diffuse background emission than the corresponding Spitzer observations. Differences between the Spitzer and WISE infrared profiles are therefore interpreted cautiously, since they may represent genuine temporal variability, but may also arise from source confusion, background emission, or survey-dependent aperture effects.

The compiled and processed SED data used in the analysis are listed in Table 1. For each photometric point, the table provides the effective wavelength, adopted flux density (or upper limit), photometric uncertainty, bandpass, number of distinct photometric records contributing to the combined value, corresponding source catalogues, observing epoch when available, uncertainty treatment, and its treatment in the SED analysis (included, excluded, or treated as an upper limit). Exact duplicate catalogue entries were removed before independent measurements within the same bandpass were combined. For records lacking a valid catalogue uncertainty, a wavelength-dependent uncertainty was assigned during the data-cleaning procedure. The uncertainties listed in Table 1 are these adopted photometric uncertainties; the additional 20% systematic term was added in quadrature separately when evaluating the SED likelihood, as described in Section 3.3.

2.2. Time-series Photometry

2.2.1. TESS Observations

CPD–82 291 was observed by TESS in eight sectors (11, 13, 38, 39, 65, 66, 93, and 94), spanning different observing epochs and cadences. The observations were obtained with exposure times of 1800s (Sectors 11 and 13), 600 s (Sectors 38 and 39), and 200 s (Sectors 65, 66, 93, and 94).

We used the Quick-Look Pipeline (QLP, Huang et al. 2020) light curves for all sectors with `lightkurve` (Lightkurve Collaboration et al. 2018) while using the quality flag setting of "hard," without applying any externally detrending, or offset correction. A total of 49,427 photometric measurements were collected from these sectors, with none rejected. The

light curves from all sectors were combined to construct a homogeneous dataset, which is shown in Figure 1.

The multi-sector data reveal a stable overall light-curve morphology, while significant variations are observed in the out-of-eclipse regions. In particular, large-amplitude wave-like modulations are present at the light-curve maxima, and the phase and shape of these modulations change from sector to sector. This behavior indicates the presence of evolving surface inhomogeneities, most likely related to stellar activity.

Furthermore, asymmetries in the secondary minimum are consistently observed in all sectors, whereas the primary eclipse remains largely unaffected. The combination of these features suggests that the system exhibits strong and time-dependent activity, which primarily influences the out-of-eclipse flux levels and the morphology of the secondary eclipse.

2.2.2. ASAS-SN Observations

In the ASAS-SN database (Shappee et al. 2014; Jayasinghe et al. 2019), CPD–82 291 is listed with the identifier ASASSN-V J085305.31−824400.0. The same astrophysical source was previously discussed by Christy et al. (2022) as ASASSN-V J085305.34−824360.0; those authors also noted the earlier *V*-band catalogue identifier ASASSN-V J085305.74−824401.0. The small differences among these coordinate-based identifiers reflect the catalogue/reference positions adopted in different ASAS-SN data products and do not correspond to distinct nearby sources.

A total of 1063 photometric measurements were obtained between 2014 May and 2021 July, consisting of 241 observations in the *V* band and 822 in the *g* band. The dataset used here was retrieved from the ASAS-SN database and overlaps the observations considered by Christy et al. (2022), although we do not assume a point-by-point identity with the light-curve extraction used in their Citizen ASAS-SN analysis. In particular, Christy et al. (2022) primarily analysed the newer *g*-band data while referring separately to the earlier *V*-band classification.

Each observation was acquired on a separate night; therefore, the dataset does not include continuous coverage during eclipse phases, making the determination of precise times of minima challenging. The *V*-band data span the period 2014–2018, whereas the *g*-band observations extend from 2017 to 2021. The phase-folded light curves in both passbands are shown in Figure 2, constructed using the ephemeris given in Equation (2).

3. Analysis

3.1. Eclipse-timing and Orbital-period Analysis

From the TESS observations, a total of 18 primary-eclipse times were determined using Kwee & van Woerden (1956). The individual timings and their uncertainties are listed in Table 2. The secondary eclipse is relatively shallow and is strongly affected by activity-related light-curve distortions; therefore, the secondary minima were not included in the eclipse-timing analysis.

A quadratic fit to the *O*–*C* data yields

$$\begin{aligned} O - C = {} & (3.63 \pm 0.31) \times 10^{-3} \\ & - (1.23 \pm 0.07) \times 10^{-4} E \\ & + (5.5 \pm 0.3) \times 10^{-7} E^2 \end{aligned} \quad (1)$$

The corresponding updated quadratic ephemeris is given by

$$\begin{aligned} T(\mathrm{HJD}) = {} & 2458603.4033 \\ & + 10.20514\, E \\ & + 5.5 \times 10^{-7} E^2. \end{aligned} \quad (2)$$

The positive quadratic term provides a phenomenological description of the curvature seen in the current *O*–*C* measurements (see Figure 3), but it should not be interpreted as secure evidence for a secular increase in the orbital period. The timing measurements are confined to a limited and temporally clustered TESS baseline, and the strong surface activity of CPD–82 291 may introduce additional systematic shifts in the measured eclipse times through distortions of the eclipse profiles. Consequently, the observed curvature could represent only part of a longer-term variation, and interpretations involving secular period evolution, magnetic activity, or the light-travel-time effect of a tertiary component cannot presently be distinguished. A longer timing baseline and quantitative comparison of alternative timing models are required to establish the physical origin of the observed trend.

3.2. Light-curve Modelling

We first modelled the Sector 94 light curve to establish a reference binary solution. Sector 94 was selected because it provides the highest-quality light curve and well-defined eclipse profiles. The remaining TESS sectors exhibit different out-of-eclipse modulations and were subsequently analysed with the reference binary parameters held fixed, as described in Section 3.4.

Although additional photometric data are available from the ASAS-SN survey in the *V* and *g* bands (see Section 2.2.2 and Figure 2), these data were not included in the light-curve modeling. Compared to the TESS observations, the ASAS-SN light curves have significantly lower photometric precision and sparse temporal sampling, limiting their ability to constrain the eclipse morphology and surface-brightness variations. We therefore used only the TESS photometry for the binary light-curve solution.

The Sector 94 light curve was modelled with the PHysics Of Eclipsing BinariEs code (`PHOEBE`, Prša & Zwitter 2005; Prša et al. 2016; Horvat et al. 2018; Jones et al. 2020; Conroy et al. 2020), version 2.4, adopting a detached binary configuration.

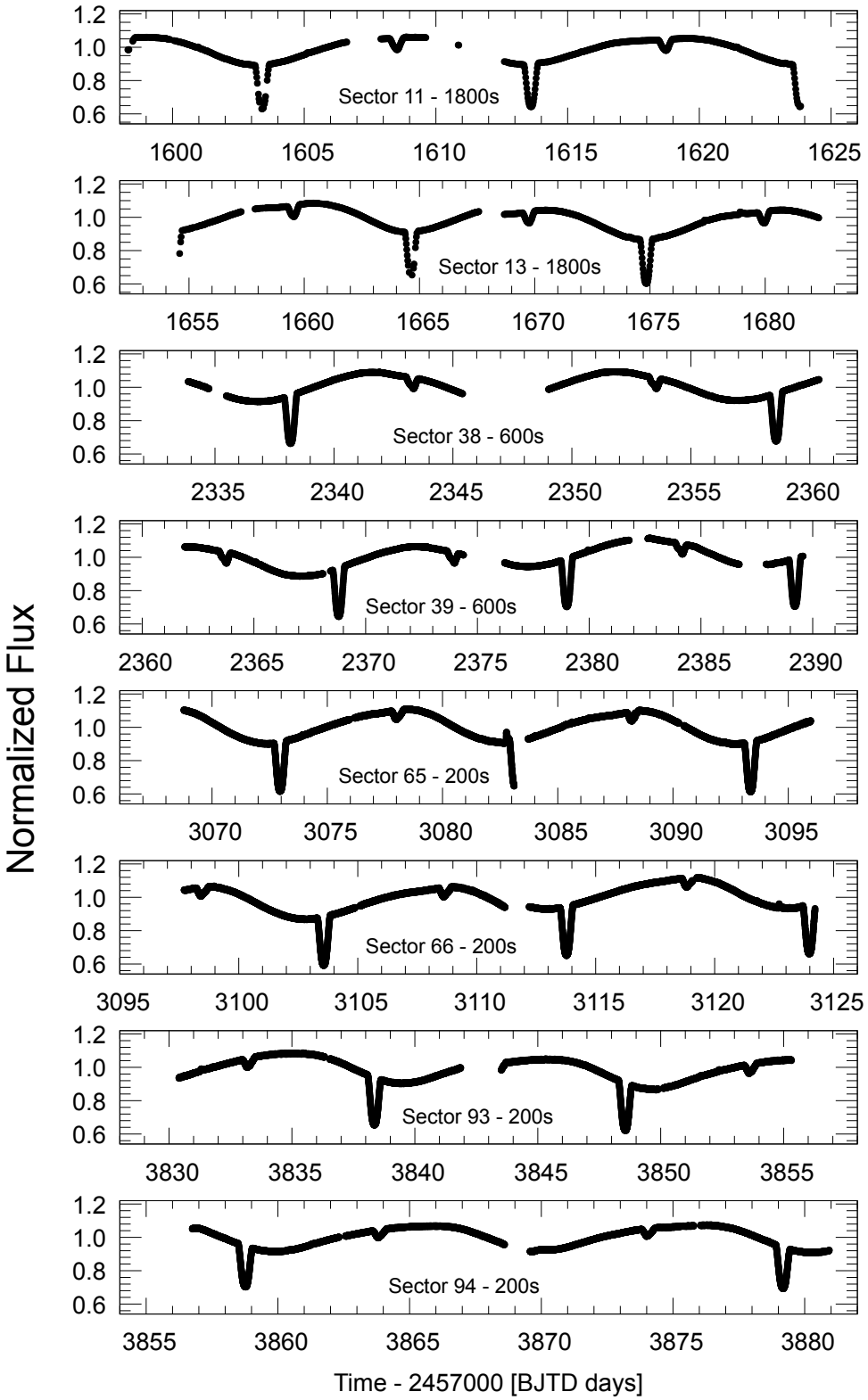


Figure 1. TESS light curves of CPD–82 291 obtained in eight different sectors with varying cadences.

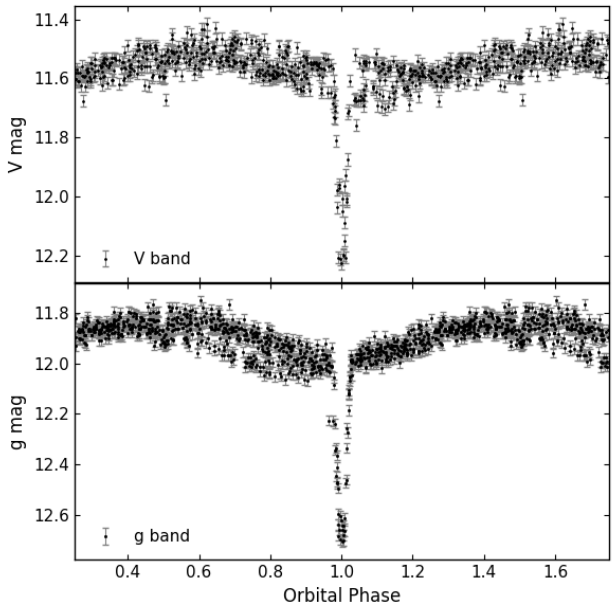


Figure 2. Phase-folded ASAS-SN light curves of CPD-82 291 in the *V* (top) and *g* (bottom) bands.

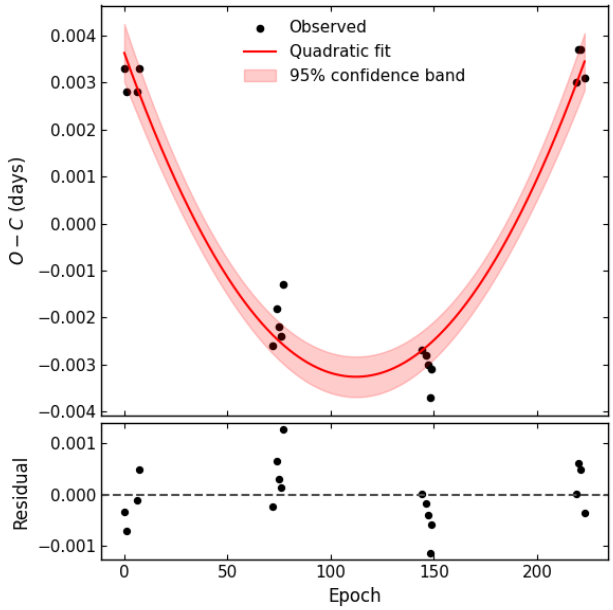


Figure 3. O–C diagram constructed from the TESS primary-eclipse timings. The solid curve represents the best-fitting quadratic model, while the shaded region denotes the 95% confidence interval of the fit.

Table 2
Calculated Times of Minima for CPD-82 291

Observed ToM HJD	Error (days)
2458603.40291	0.00087
2458613.60774	0.00051
2458664.63403	0.00127
2458674.83977	0.00043
2459338.17604	0.00017
2459358.58730	0.00011
2459368.79215	0.00016
2459378.99722	0.00019
2459389.20361	0.00012
2460072.95482	0.00009
2460093.36529	0.00010
2460103.57034	0.00008
2460113.77488	0.00010
2460123.98078	0.00015
2460838.35533	0.00009
2460848.56124	0.00010
2460858.76658	0.00013
2460879.17644	0.00017

The adjustable parameters included the volume-equivalent fractional radii, photometric mass ratio, orbital inclination, component temperature ratio, and luminosity contribution in the TESS bandpass.

The third-light contribution was initially included as a free parameter to test for unresolved contaminating flux. Trial solutions converged to negligible values of $l_3 \simeq 0.001$–0.002, without a meaningful improvement in the fit. We therefore fixed $l_3 = 0$ in the final solution. This test constrains only additional flux in the photometric aperture and does not by itself test for the dynamical presence of a tertiary component.

The primary effective temperature adopted in the light-curve calculation does not represent an independent temperature measurement from the TESS data. It sets the reference temperature scale used by `PHOEBE` for the stellar-atmosphere, passband-intensity, and limb-darkening calculations, whereas the principal temperature constraint provided by the light curve is the component temperature ratio. The absolute effective temperatures of both components are subsequently determined from the SED analysis while preserving the temperature ratio obtained from the light-curve solution (Section 3.3).

Although the model was sampled using $T_{\rm eff,1}/T_{\rm eff,2}$, its reciprocal, $T_{\rm eff,2}/T_{\rm eff,1}$, is reported in Table 3 for consistency with the notation used in the SED analysis. The parameters allowed to vary during the optimization, together with the fixed model inputs and their adopted values or sources, are listed separately in Table 3.

Before performing the Markov chain Monte Carlo (MCMC, Foreman-Mackey et al. 2013) analysis to obtain fundamental parameters and uncertainties, we carried out a preliminary photometric mass-ratio search to identify the region of parameter space providing the best light-curve solution. The mass ratio was fixed at successive values over the interval

Table 3
Light-curve Solution Parameters Derived from the TESS Sector 94 Data Using PHOEBE v2.4

Parameter	Value	Source/Assumption
Fitted parameters		
Primary fractional radius, r_1	$0.0568^{+0.0050}_{-0.0050}$	MCMC
Secondary fractional radius, r_2	$0.1687^{+0.0050}_{-0.0050}$	MCMC
Photometric mass ratio, $q = M_2/M_1$	$0.4638^{+0.0126}_{-0.0097}$	MCMC
Orbital inclination, i (°)	$82.1^{+0.057}_{-0.069}$	MCMC
Temperature ratio, $T_{\rm eff,2}/T_{\rm eff,1}$	$0.6413^{+0.0031}_{-0.0026}$	MCMC
Primary *TESS* light fraction, $l_{1,\rm TESS}$	$0.342^{+0.004}_{-0.003}$	MCMC
Fixed parameters and assumptions		
Orbital period, P (d)	10.20514	Eclipse-timing analysis
Reference epoch, T_0 ($\rm BJD_{TDB}$)		2458613.642535
Eclipse-timing analysis		
Eccentricity, e	0	Circular orbit adopted
Adopted primary effective temperature, $T_{\rm eff,1}$ (K)	6900	Ref. temp. for atm. and LD calculations
Bolometric albedos, $A_{1,2}$	0.500	Convective envelopes
Gravity-darkening exponents, $g_{1,2}$	0.320	Convective envelopes
Third light, l_3	0	Adopted
Synchronicity parameters, $F_{1,2}$	1.0	Synchronous rotation adopted
TESS LD coefficient, x_1	0.640	Adopted LD tables
TESS LD coefficient, y_1	0.361	Adopted LD tables
TESS LD coefficient, x_2	0.738	Adopted LD tables
TESS LD coefficient, y_2	0.257	Adopted LD tables
Bolometric LD coefficient, $x_{\rm Bol,1}$	0.681	Adopted LD tables
Bolometric LD coefficient, $y_{\rm Bol,1}$	0.184	Adopted LD tables
Bolometric LD coefficient, $x_{\rm Bol,2}$	0.714	Adopted LD tables
Bolometric LD coefficient, $y_{\rm Bol,2}$	0.045	Adopted LD tables
Derived parameters		
Secondary TESS light fraction, $l_{2,\rm TESS}$	$0.658^{+0.003}_{-0.004}$	$1 - l_{1,\rm TESS}$, assuming $l_3 = 0$

Note. Quoted uncertainties represent the 16th and 84th percentiles of the posterior distributions. The mass ratio is photometric and model dependent.

$0.30 \leqslant q \leqslant 0.70$, while the remaining adjustable light-curve parameters were re-optimized at each trial value. The goodness of fit was evaluated using the corresponding χ^2 value. As shown in Figure 4, the χ^2 distribution reaches its minimum near $q = 0.46$, while the quality of the fit deteriorates toward both smaller and larger mass ratios.

The value obtained from this preliminary search was used only as the initial estimate for the subsequent MCMC analysis. In the MCMC calculation, q was allowed to vary freely together with the other fitted binary parameters. The resulting posterior solution, $q_{\rm phot} = 0.4638^{+0.0126}_{-0.0097}$, is consistent with the minimum of the independent q-search. Because the system is

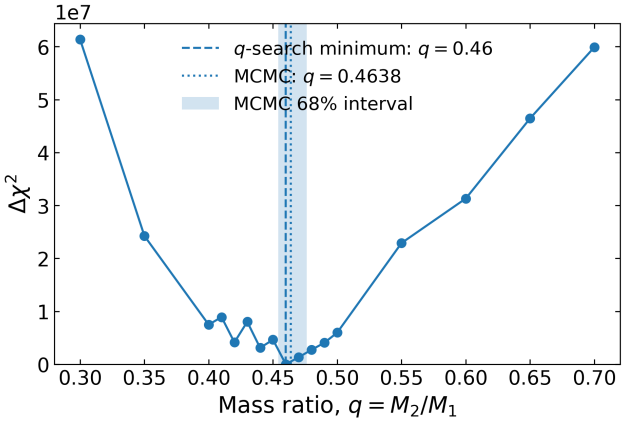


Figure 4. Photometric mass-ratio search for CPD–82 291. The ordinate shows $\Delta\chi^2 = \chi^2 - \chi^2_{\rm min}$ obtained by fixing the mass ratio at successive trial values and re-optimizing the remaining adjustable light-curve parameters. The minimum occurs near $q = 0.46$. The vertical dotted line and shaded interval indicate the median and 68% credible interval of the subsequent MCMC solution, $q_{\rm phot} = 0.4638^{+0.0126}_{-0.0097}$.

detached and its out-of-eclipse light curve is strongly affected by surface-brightness inhomogeneities, this value is treated as a photometric and model-dependent mass ratio rather than a direct dynamical measurement. An independent spectroscopic orbit is required to determine the dynamical mass ratio and to assess possible systematic uncertainties associated with the adopted surface-brightness model.

Parameter uncertainties were estimated through a MCMC analysis with 128 walkers and 1000 iterations. The parameters identified as fitted in Table 3, including the photometric mass ratio, were allowed to vary. The posterior medians and corresponding 16th and 84th percentiles were adopted as the parameter estimates and their 68% credible intervals. The quoted intervals describe the statistical uncertainties within the adopted light-curve and surface-brightness model and do not include all possible systematic uncertainties associated with the fixed assumptions.

The median posterior model for Sector 94 is shown in Figure 5, and the corresponding parameter values are summarized in Table 3. The posterior distributions and parameter correlations are shown in the corner plot in Appendix B, Figure A2.

3.3. SED Modelling

The SED of the system was first modelled using the stellar photospheres alone and was subsequently compared with a model including an additional circumstellar dust component. The total observed flux was represented as

$$F_\nu^{\rm obs} = (F_{\nu,1} + F_{\nu,2} + F_{\nu,\rm disk})\,10^{-0.4A_\lambda}, \quad (3)$$

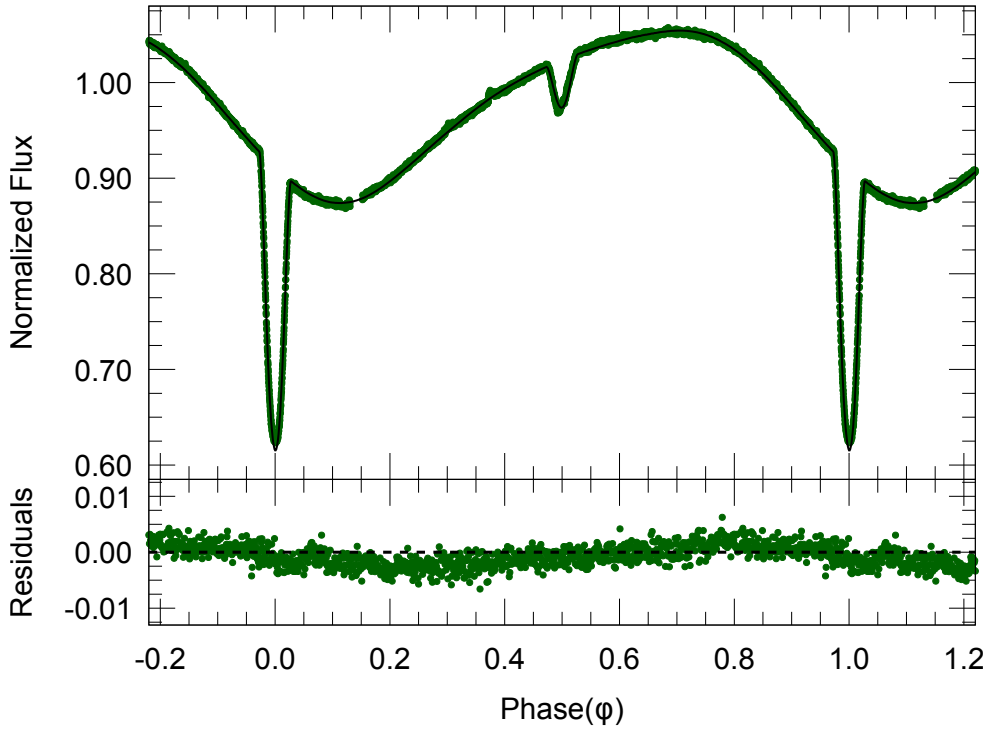


Figure 5. TESS Sector 94 light curve and the corresponding median posterior model obtained with PHOEBE v2.4. The lower panel shows the residuals, $O-C$.

where $F_{\nu,1}$ and $F_{\nu,2}$ are the contributions from the primary and secondary components, respectively, and $F_{\nu,\mathrm{disk}}$ is the thermal emission from the adopted disk model. For the stellar-only solution, $F_{\nu,\mathrm{disk}}$ was set to zero. The disk component was included only to investigate whether the tentative far-infrared emission could be reproduced by a cool circumbinary-dust model. The extinction was parameterized through the colour excess $E(B-V)$ using the G23 extinction law (Gordon et al. 2023), with $R_V = 3.1$.

The stellar fluxes were represented by blackbody spectra,

$$F_{\nu,\star} = \left(\frac{R_\star}{d}\right)^2 \pi B_\nu(T_\star), \tag{4}$$

where $R_\star$ and $T_\star$ are the stellar radius and effective temperature, respectively, and d is the distance to the system. The distance was fixed at $d = 486.9 \pm 3.2$ pc, obtained by direct inversion of the source-dependent zero-point-corrected Gaia DR3 parallax, $\varpi_{\mathrm{corr}} = 2.0538 \pm 0.0134$ mas. The component temperature and radius ratios were fixed to the posterior medians obtained from the light-curve analysis,

$$\frac{T_{\star,2}}{T_{\star,1}} = 0.6413, \qquad \frac{R_{\star,2}}{R_{\star,1}} = 2.971. \tag{5}$$

Fixing the light-curve temperature and radius ratios reduces the stellar part of the SED model from four independent parameters ($T_{\star,1}$, $T_{\star,2}$, $R_{\star,1}$, and $R_{\star,2}$) to two ($T_{\star,1}$ and $R_{\star,1}$), while the Gaia distance provides an external scale constraint. These constraints restrict the allowed stellar parameter space but do not eliminate the remaining covariances among stellar temperature, radius, and reddening. They also do not independently establish the presence or geometry of a circumbinary disk.

The disk emission was calculated by integrating the thermal emission from concentric annuli,

$$F_{\nu,\mathrm{disk}} = \frac{\cos i_{\mathrm{disk}}}{d^2} \int_{R_{\mathrm{in}}}^{R_{\mathrm{out}}} 2\pi r B_\nu[T(r)] \times \left[1 - \exp\left(-\frac{\tau_\nu(r)}{\cos i_{\mathrm{disk}}}\right)\right], dr. \tag{6}$$

The radial structure follows the parametrized model presented by Bakış & Habalı (2026), incorporating a power-law surface-density distribution and a passive irradiation temperature profile. The model was extended to include the combined irradiation from both stellar components.

Because the disk is spatially unresolved, its inclination cannot be determined independently from the SED. We therefore adopted $i_{\mathrm{disk}} = i_{\mathrm{binary}} = 82.^\circ1$ as a fiducial coplanar configuration. To examine the sensitivity to this assumption, the deterministic optimization was repeated for fixed inclinations of

0°, 30°, 60°, and 82.°1. These tests used the same revised likelihood as the fiducial analysis, including the 60 μm flux measurement and the one-sided 90 μm upper-limit constraint. The corresponding total χ^2 values were 6.778, 6.778, 6.778, and 6.779, respectively.

The stellar parameters and inner disk radius remained broadly similar, whereas the surface-density normalization decreased from approximately 0.30 g cm^{-2} at 0° to 0.050 g cm^{-2} at 82.°1, a change by a factor of about six. In these deterministic sensitivity tests, the optimizer converged to outer radii close to the adopted lower boundary ($R_{\rm out} \simeq$ 105–107 au) for all four inclinations. This behaviour should not be interpreted as a posterior constraint on $R_{\rm out}$: in the fiducial $i_{\rm disk} = 82.^\circ1$ MCMC analysis, the posterior is broad and asymmetric, with $R_{\rm out} = 188^{+150}_{-52}$ au. The difference between the deterministic optimum and the posterior distribution further illustrates the weak constraint on the outer disk radius. These tests show that the unresolved photometry does not independently constrain the disk inclination and that the inferred surface density, dust mass, and radial extent remain model dependent.

We used the cleaned and band-combined photometric measurements described in Section 2.1. To account for cross-survey calibration differences, non-simultaneous observations, source variability, and limitations of the adopted photospheric and disk prescriptions, a fractional systematic uncertainty equal to 20% of the measured flux was added in quadrature to the adopted uncertainty of each fitted measurement:

$$\sigma_{\nu,\rm eff} = \sqrt{\sigma^2_{\nu,\rm phot} + (0.20F_\nu)^2}\,. \tag{7}$$

Here, $\sigma_{\nu,\rm phot}$ denotes either the combined catalogue uncertainty described in Section 2.1 or the adopted uncertainty for measurements lacking a valid catalogue error. This conservative prescription prevents measurements with very small formal errors from dominating the broadband fit.

Special treatment was applied to the far-infrared measurements reported by Spangler et al. (2001). The 60 μm value, $F_{60} = 0.026 \pm 0.019$ Jy, was included in the conditional disk fit as a flux measurement with its published uncertainty, but its significance of only 1.37σ was not regarded as a secure detection. The 90 μm non-detection was represented by a 3σ upper limit of 0.021 Jy, corresponding to $\sigma_{\nu,\rm ul} = 0.007$ Jy. Its contribution to the likelihood was implemented through the one-sided term

$$\chi^2_{\rm ul} = \left[\max\left(0, \frac{F_{\nu,\rm model} - F_{\nu,\rm lim}}{\sigma_{\nu,\rm ul}}\right)\right]^2, \tag{8}$$

so that no penalty was applied when the model remained below the upper limit.

The best-fitting parameters were initially determined through non-linear least-squares optimization. The stellar-only model included $T_{\star,1}$, $R_{\star,1}$, and $E(B-V)$ as free parameters. For the conditional disk solution, Σ_0, $R_{\rm in}$, and $R_{\rm out}$ were additionally varied. All other quantities were held fixed at the values listed in Table 4.

The best-fitting stellar-plus-disk solution was then used to initialize an MCMC analysis. The MCMC sampling was used to characterize the posterior distributions and parameter correlations within the adopted conditional disk model. Uniform priors were adopted within the parameter boundaries

Table 4
Parameters of the Stellar SED and Conditional Circumbinary-dust Model

Parameter	Value	Prior
	Fitted parameters	
$T_{\star,1}$ (K)	6898^{+670}_{-480}	$\mathcal{U}$(5020, 8020)
$R_{\star,1}$ ($R_\odot$)	$1.245^{+0.094}_{-0.087}$	$\mathcal{U}$(0.666, 1.997)
Σ_0 (g cm^{-2})	$0.0256^{+1.0}_{-0.022}$	$\mathcal{U}(10^{-5}, 2)$
$R_{\rm in}$ (AU)	147^{+37}_{-48}	$\mathcal{U}$(10, 200)
$R_{\rm out}$ (AU)	188^{+150}_{-52}	$\mathcal{U}$(100, 500)
$E(B-V)$	$0.130^{+0.110}_{-0.089}$	$\mathcal{U}$(0, 1)
	Fixed parameters and model inputs	
$T_{\star,2}/T_{\star,1}$	0.6413	⋯
$R_{\star,2}/R_{\star,1}$	2.970	⋯
Gaia DR3 parallax, ϖ (mas)	2.0365 ± 0.0134; corr. 2.0538 ± 0.0134	⋯
Distance, d (pc)	486.9 ± 3.2	⋯
Disk inclination, $i_{\rm disk}$ (°)	82.1	⋯
Stellar photosphere model	Blackbody	⋯
Extinction law; R_V	G23 (Gordon et al. 2023); 3.1	⋯
Systematic photometric uncertainty	0.20 F_ν	⋯
Disk scale height, H_0 (AU)	0.03	⋯
Surface-density exponent, p_Σ	1.0	⋯
Disk flaring exponent, β_H	1.1	⋯
Dust opacity (κ_0, λ_0, β_κ)	(0.5, 100 μm, 1.25)	⋯
	Derived parameters	
$T_{\star,2}$ (K)	4423^{+430}_{-308}	⋯
$R_{\star,2}$ ($R_\odot$)	$3.697^{+0.279}_{-0.258}$	⋯
A_V (mag)[a]	$0.403^{+0.341}_{-0.276}$	⋯
$M_{\rm dust}$ ($M_\odot$)	$(8.1^{+16.0}_{-5.7}) \times 10^{-5}$	⋯

Notes. Uncertainties are the 16th and 84th percentiles of the MCMC posterior distributions. Uniform priors are listed for fitted parameters; disk quantities are conditional and model dependent.
The temperature and radius ratios are adopted from the light-curve solution. The Gaia distance is based on the zero-point-corrected parallax ($Z_\varpi = -0.0173$ mas) and was held fixed in the SED fit. The disk inclination was fixed at 82.°1 assuming coplanarity.
[a] $A_V = R_V E(B-V)$ with $R_V = 3.1$.

listed in Table 4, with the additional physical requirement $R_{\rm out} - R_{\rm in} \geqslant 1$ au. No Gaussian or other informative prior was imposed on $E(B - V)$.

The posterior sampling was performed with the `emcee` affine-invariant ensemble sampler using 32 walkers. The walkers were initialized in the vicinity of the deterministic least-squares solution with a dispersion corresponding to 2% of the allowed range of each fitted parameter; all initial walker positions were required to satisfy the adopted priors. The sampler was allowed to run for a maximum of 70,000 steps per walker.

Convergence was assessed from the integrated autocorrelation time, τ, estimated separately for each fitted parameter at intervals of 5000 steps. Sampling was considered practically converged when the total chain length exceeded 50τ for every parameter and the maximum fractional change in the estimated autocorrelation times between successive checks was less than 5%. These criteria were satisfied after 50,000 steps. The final integrated autocorrelation times ranged from 393.7 to 970.7 steps, corresponding to a minimum chain-length-to-autocorrelation-time ratio of 51.5. The maximum fractional change in τ at the final convergence check was 2.5%.

After convergence was established, the first 4854 steps were discarded as burn-in, corresponding to approximately five times the largest integrated autocorrelation time. The retained chains were thinned by a factor of 196, approximately one half of the shortest autocorrelation time, yielding 7360 posterior samples used for parameter estimation.

The mean acceptance fraction of the converged run was 0.192. This quantity is reported as a sampling diagnostic and was not used as evidence of convergence. The posterior medians and the corresponding 16th and 84th percentiles were adopted as the parameter estimates and 68% credible intervals. These intervals describe the allowed parameter ranges within the conditional disk model and do not constitute evidence for the existence of the disk.

As an additional assessment of the adequacy of the fitted model, posterior-predictive realizations were generated from samples drawn from the converged posterior distribution. For each posterior draw, the model SED was evaluated at the observed wavelengths and synthetic measurements were generated using the same effective uncertainty prescription adopted in the likelihood.

Using the revised photometric uncertainties and the additional 20% systematic term defined above, the residuals were evaluated quantitatively using the same effective uncertainties adopted in the SED likelihood. Relative to the stellar-only photospheric model, the W3 and W4 measurements differ from the model by approximately -0.39σ and -0.37σ, respectively, while the 60 μm measurement lies only $+1.30\sigma$ above the stellar prediction. Thus, the photometry through WISE W4 is consistent with the stellar photospheres, and the 60 μm point represents only a low-significance positive far-infrared deviation.

As a separate diagnostic test of whether the shorter-wavelength SED itself requires an additional dust component, the W4 and 60 μm measurements were excluded from both models, leaving 30 photometric points in the comparison dataset. This diagnostic comparison is distinct from the conditional disk fit described above, in which W4 and the 60 μm measurement were retained and the 90 μm upper limit was applied. The stellar-only model, with three free parameters, yielded $\chi^2 = 5.830$ for 27 degrees of freedom ($\chi^2_\nu \simeq 0.22$). The low value of χ^2_ν is expected in part from the deliberately conservative 20% systematic uncertainty included in the likelihood and should not be interpreted as evidence for an exceptionally precise model.

The stellar-plus-disk model yielded essentially the same χ^2 despite introducing three additional free parameters. The stellar-only solution gives $\mathrm{AIC_c} = 12.75$ and $\mathrm{BIC} = 16.03$, compared with $\mathrm{AIC_c} = 21.48$ and $\mathrm{BIC} = 24$ for the stellar-plus-disk model. Thus, $\Delta\mathrm{AIC_c} = 8.73$ and $\Delta\mathrm{BIC} = 10.20$ favour the stellar-only model, while the disk parameters become poorly constrained when the tentative long-wavelength measurements are removed. The optical-to-W3 photometry therefore does not require an additional circumstellar-dust component.

The observed SED and the two model representations are shown in Figure 6. The MCMC parameter estimates are listed in Table 4, and their posterior distributions are presented in Appendix B, Figure A6. The physical interpretation and limitations of the conditional disk solution are discussed in Sections 4.2.1 and 4.4.

3.4. Sector-by-sector Surface-brightness Modelling

To characterize the changing out-of-eclipse modulations, we modelled the light curves from Sectors 11, 13, 38, 39, 65, 66, 93, and 94 separately. The orbital and stellar parameters were fixed to the reference solution derived from Sector 94 (Section 3.2), because these parameters are not expected to vary over the time span of the observations. Only the parameters describing the surface-brightness inhomogeneities were adjusted between the individual data segments.

The same parametrized configuration was adopted for all segments, consisting of one circular surface-brightness region on the secondary component and two regions on the primary. For each region, the spot-to-local-surface temperature ratio, colatitude, longitude, and angular radius were allowed to vary. The suffixes "–1" and "–2" in Table 5 denote the temporal subdivisions of the corresponding sectors. The observation baseline of TESS is approximately 27 days per sector. Given the orbital period of CPD-82 291 of $\sim$10 days, each sector covers approximately two orbital cycles. We therefore analyzed the individual cycles within each sector independently.

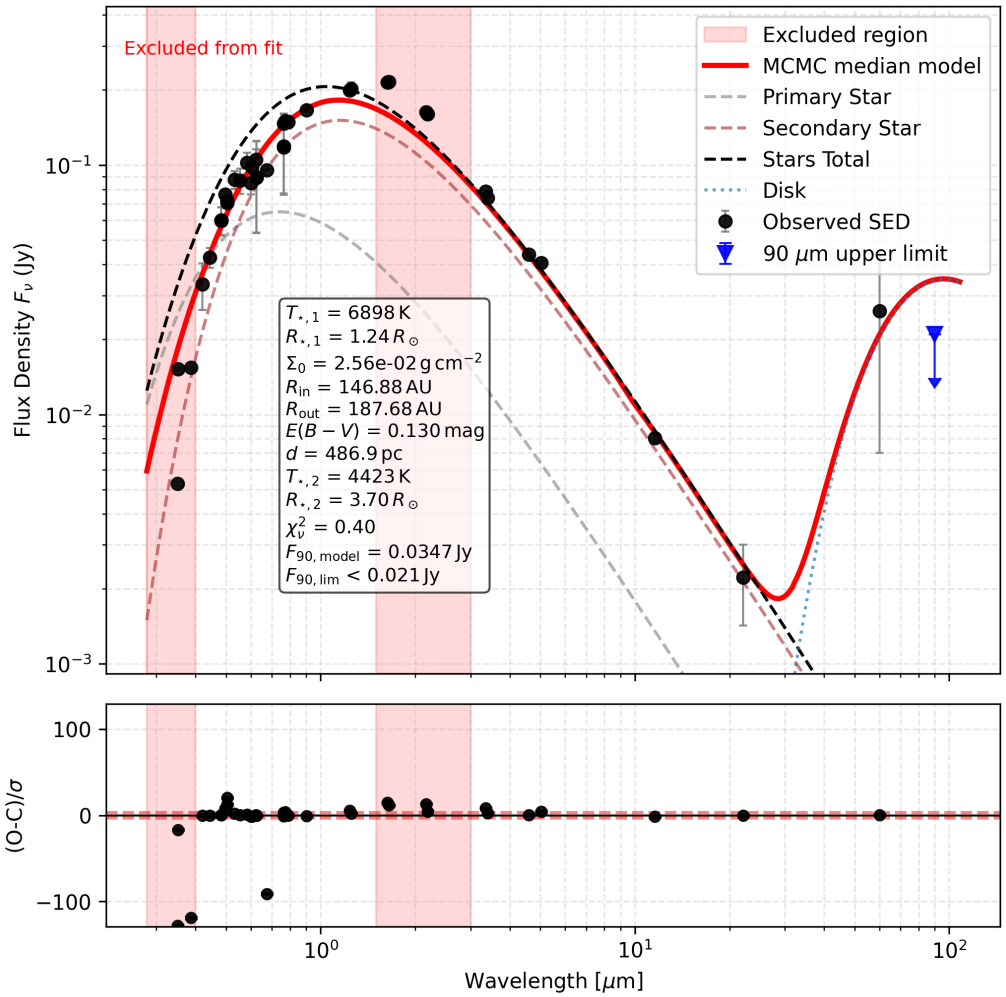


Figure 6. Observed SED and model comparison. Top panel: The photometric measurements are shown together with the stellar-only model (black dashed line) and the conditional stellar-plus-disk model (red solid line), as identified in the legend. The stellar photospheres reproduce the SED through the WISE W4 band, and neither W3 nor W4 shows a significant infrared excess. The additional disk component illustrates one possible interpretation of the low-significance 60 μm measurement. The blue downward arrow denotes the 90 μm upper limit and does not represent a flux detection. Shaded regions indicate wavelength intervals excluded from the main SED fitting procedure for the reasons described in the text. Bottom panel: Normalized residuals $(O-C)/\sigma$ computed using the revised effective uncertainties adopted in the SED likelihood. The W3 and W4 measurements remain consistent with the stellar photospheric contribution, while the 60 μm point represents only a low-significance positive deviation. The disk model is conditional and should not be interpreted as a unique determination of the disk properties.

The spot angular radius, $\alpha_{\rm spot}$, denotes the angular radius of the circular cap used to represent an individual surface-brightness region on the stellar surface; it is therefore an angular size rather than a physical radius in units of $R_\odot$. For an individual circular cap, the fraction of the total stellar surface covered by the region is $f_{\rm spot} = (1 - \cos\alpha_{\rm spot})/2$. Thus, angular radii of 65°–82° correspond to individual surface-covering fractions of approximately 29%–43%. These fractions should not be interpreted as a unique total spotted area when multiple regions are present. The large fitted regions should instead be regarded as a parametrization of the asymmetric surface-brightness distribution rather than as uniquely determined individual physical spots.

The circular regions used in the model should be regarded as a parametrized representation of large-scale surface-brightness inhomogeneities rather than as unique maps of individual physical spots. Their fitted sizes, temperature contrasts, and positions are mutually degenerate and may represent combinations of multiple unresolved active regions.

The best-fitting parameters obtained for the individual segments are listed in Table 5, and their sector-to-sector variation is shown in Figure 7. Representative model surfaces

Table 5
Fitted Spot Parameters Obtained from the Sector-by-sector Light-curve Solutions, Illustrating the Temporal Changes in the Parametrized Surface-brightness Distributions

Sector	Mid-BJTD	Secondary Spot				Primary Spot 1				Primary Spot 2			
		$T_{\rm rel}$	Colat. (deg)	Long. (deg)	Rad. (deg)	$T_{\rm rel}$	Colat. (deg)	Long. (deg)	Rad. (deg)	$T_{\rm rel}$	Colat. (deg)	Long. (deg)	Rad. (deg)
Sector11-2	8613.61	0.9602	92.4601	195.1268	66.4772	0.9413	89.3431	189.4455	18.7151	1.3785	92.0224	174.5958	18.2822
Sector13-1	8664.63	0.9570	94.5761	190.9004	66.3762	0.9416	89.2880	189.4982	18.7085	1.3799	91.9399	173.5865	18.4206
Sector13-2	8674.84	0.9516	92.2384	187.3188	66.3807	0.9417	89.2708	189.4340	18.7021	1.3801	91.9368	173.6960	18.4200
Sector38-1	9338.18	0.9544	92.2557	238.7179	66.3370	0.9411	89.4494	249.5484	18.7081	1.3636	91.8946	233.6335	18.4076
Sector38-2	9358.59	0.9546	92.5193	245.6491	66.3677	0.9424	89.4187	249.4313	18.7073	1.3656	91.8978	235.4834	18.4081
Sector39-1	9368.79	0.9483	92.2652	246.4660	65.7037	0.9212	89.4030	251.1126	18.7621	1.3902	91.8030	235.7709	18.4009
Sector39-2	9379.00	0.9526	91.9191	246.4698	65.6879	0.9188	89.3107	249.0609	18.7070	1.3283	91.6347	232.7646	18.4475
Sector65-1	10072.95	0.9518	91.8628	203.2935	82.6160	0.9451	88.6403	260.0475	17.3238	1.4289	89.8332	158.5490	18.4915
Sector65-2	10093.37	0.9509	91.8863	212.3859	81.8096	0.9204	88.9056	259.7706	17.2947	1.4266	88.7743	157.5119	17.8060
Sector66-1	10103.57	0.9466	93.3694	207.1445	79.7251	0.9422	89.1131	258.0376	17.2638	1.3221	88.7337	157.4687	17.8828
Sector66-2	10113.77	0.9541	91.8508	212.5278	81.6854	0.9201	88.9371	259.7188	17.2761	1.3594	88.6679	157.6116	17.7987
Sector93-1	10838.36	0.9290	90.0129	137.9898	66.8479	0.9399	89.0158	212.0375	47.7732	0.8250	90.0095	77.2543	18.2667
Sector93-2	10848.56	0.9271	90.8100	137.8200	66.8600	0.9400	88.9300	212.5000	46.5800	0.8249	90.2300	77.3000	18.1500
Sector94-1	10858.77	0.9413	90.0122	138.0094	66.9009	0.9400	89.0113	212.0173	46.5984	0.8250	90.0013	77.0279	18.1516
Sector94-2	10879.18	0.9374	90.0356	137.9923	66.9174	0.9403	89.0078	212.0714	46.5678	0.8249	90.0100	77.0275	18.1542

Note. Mid-times are given as BJD − 2450000. The tabulated quantities are $T_{\rm rel}$, the spot-to-local-surface temperature ratio; Colat., the fitted spot colatitude; Long., the fitted spot longitude; and Rad., the angular radius of the circular cap adopted in the spot model. These parameters describe a non-unique representation of the observed light-curve asymmetries and should not be interpreted as direct measurements of the size, location, or evolution of individual physical spots.

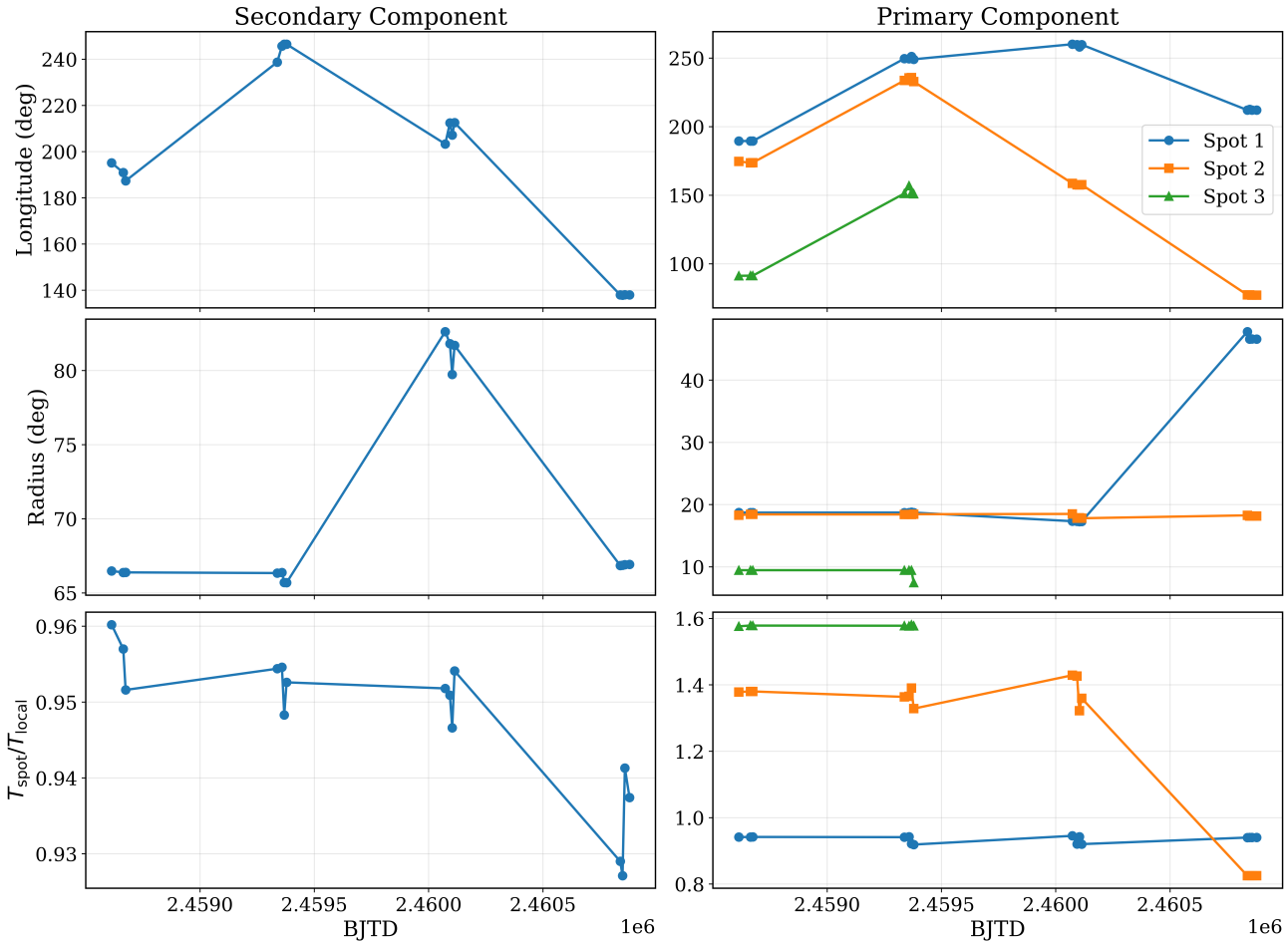


Figure 7. Temporal evolution of the spot parameters obtained from the sector-by-sector light-curve solutions. The left and right columns show the spot parameters for the secondary and primary components, respectively. From top to bottom, the panels show the spot longitude, angular radius, and relative temperature ($T_{\rm spot}/T_{\rm local}$). The variations indicate that the surface activity pattern changes between different TESS observing epochs.

at four orbital phases are presented in Appendix B, Figures A1–A2. These surfaces illustrate the adopted parametrized solutions and should not be interpreted as uniquely reconstructed stellar maps.

The sector-specific solutions require different surface-brightness configurations to reproduce the observed out-of-eclipse asymmetries. The physical interpretation and limitations of these changes are discussed in Section 4.3.

3.5. Flare Identification and Measurement

The flare events were identified and analyzed using an interactive procedure applied to the TESS light curves. First, a baseline model was constructed by selecting flare-free regions and fitting a low-order polynomial to remove long-term trends. For each candidate event, the selected flare-free regions surrounding the event were used to represent the local quiescent baseline, F_q. The detrended light curve was then expressed in terms of the relative excess flux,

$$\frac{F - F_q}{F_q} = \frac{F}{F_q} - 1, \tag{9}$$

thereby removing the local brightness variation while preserving the fractional flare amplitude.

Flare candidates were selected manually in the detrended data, ensuring that both the rise and decay phases were included. The selected windows were sufficiently wide to include the rise, peak, and decay portions of each event. The start and end times of each flare were determined using a threshold-based approach, with the local noise level, σ, estimated from the relative residual flux in the selected flare-free baseline regions. The first and last points exceeding 2.5σ within the candidate window were adopted as the flare start and end times, respectively. We therefore refer to the corresponding interval as the threshold-defined duration, rather than as an intrinsic physical flare duration.

The flare peak was identified as the maximum residual flux within the selected region. The observed flare amplitude was defined as the maximum relative excess flux. The flare duration was defined as the time interval between the start and end points, while the equivalent duration was calculated by integrating the flare excess flux above the baseline. Specifically, the equivalent duration was calculated directly from the observed relative excess flux as

$$\mathrm{ED} = \int \frac{F - F_q}{F_q}\, dt, \tag{10}$$

where the integration was performed over the manually selected flare interval.

Rather than approximating the flare profiles with symmetric Gaussian functions, we fitted the continuous analytic white-light flare template of Tovar Mendoza et al. (2022). The model describes the characteristic rapid heating and asymmetric cooling morphology of classical stellar flares and is parameterized by the flare peak time, amplitude, and full width at half maximum (FWHM). To account for the finite integration time of the TESS observations, the analytic profile was evaluated at a higher temporal resolution and subsequently averaged to the cadence of the corresponding light curve before comparison with the observations. This treatment is particularly relevant for the sectors obtained at relatively long cadence.

The equivalent duration obtained by integrating the best-fitting analytic template was also retained as a model-dependent diagnostic. For events whose morphology departs from that of a single classical flare, the directly integrated equivalent duration provides the less model-dependent measurement.

Figures 8 and 9 show the relative excess-flux profiles and best-fitting analytic templates for all 28 flare events identified in the TESS observations.

A total of 28 flare events were retained in the final sample. All measured parameters, including start time, peak time, threshold-defined duration, amplitude, equivalent duration, and the peak time, amplitude, and FWHM obtained from the analytic flare-template fit, were compiled into a flare catalog for further statistical analysis.

4. Results and Discussion

4.1. Binary Configuration and Model-inferred Absolute Parameters

The reference light-curve solution derived from the TESS Sector 94 photometry constrains the orbital inclination, volume-equivalent fractional radii, component temperature ratio, luminosity ratio, and photometric mass ratio. These quantities describe the relative geometry and surface-brightness distribution of the system, but the light curve alone does not determine its absolute physical scale.

The absolute radius scale was obtained by combining the light-curve constraints with the primary radius derived from the SED analysis using the adopted Gaia distance. Because no radial-velocity orbit is available, the resulting component masses and orbital dimensions are not direct dynamical measurements. They should instead be regarded as model-inferred quantities that depend on the SED radius scale, the light-curve geometry, and the photometric mass ratio.

The light-curve solution provides the volume-equivalent fractional radii,

$$r_1 = \frac{R_1}{a}, \qquad r_2 = \frac{R_2}{a}, \tag{11}$$

where a is the orbital semimajor axis. The semimajor axis was therefore calculated from the primary radius as

$$a = \frac{R_1}{r_1}. \tag{12}$$

The secondary radius was independently obtained from the light-curve radius ratio,

$$R_2 = R_1 \frac{r_2}{r_1}. \tag{13}$$

The total system mass was then inferred from Kepler's third law,

$$M_{\mathrm{tot}} = M_1 + M_2 = \frac{4\pi^2 a^3}{GP^2}, \tag{14}$$

and the individual component masses were calculated using the photometric mass ratio, $q_{\mathrm{phot}} = M_2/M_1$:

$$M_1 = \frac{M_{\mathrm{tot}}}{1 + q_{\mathrm{phot}}}, \qquad M_2 = \frac{q_{\mathrm{phot}} M_{\mathrm{tot}}}{1 + q_{\mathrm{phot}}}. \tag{15}$$

The corresponding surface gravities were calculated from

$$g_j = \frac{GM_j}{R_j^2}, \qquad j = 1, 2. \tag{16}$$

Combining Equations (12)–(15), the dependence of the inferred component masses on the directly adopted quantities can be written explicitly as

$$M_1 = \frac{4\pi^2}{GP^2}\left(\frac{R_1}{r_1}\right)^3 \frac{1}{1 + q_{\mathrm{phot}}}, \tag{17}$$

$$M_2 = \frac{4\pi^2}{GP^2}\left(\frac{R_1}{r_1}\right)^3 \frac{q_{\mathrm{phot}}}{1 + q_{\mathrm{phot}}}. \tag{18}$$

Uncertainties in the absolute radii, semimajor axis, component masses, and surface gravities were propagated through Monte Carlo sampling of the posterior distributions of R_1, r_1, r_2, and q_{phot}, together with the orbital-period uncertainty. For each Monte Carlo realization, a, R_2, M_{tot}, M_1, M_2, g_1, and g_2 were recalculated sequentially using Equations (12)–(16). Full parameter vectors were drawn from the corresponding SED



Figure 8. Relative excess-flux profiles of the first 14 flare candidates identified in the TESS observations of CPD–82 291. Points show the detrended TESS measurements and the solid curves show the best-fitting continuous analytic flare templates. Time is expressed relative to the fitted template peak. The different sampling densities reflect the cadence of the corresponding TESS observations.

and light-curve posterior samples so that correlations among parameters within each analysis were retained. Because the light-curve and SED analyses were performed separately, no additional covariance between the two posterior samples was assumed. The reported values and uncertainties were obtained from the median and the 16th and 84th percentiles of the resulting derived distributions.

Using the current posterior solution, the component radii are $R_1 = 1.245^{+0.094}_{-0.087}\,R_\odot$ and $R_2 = 3.70^{+0.29}_{-0.27}\,R_\odot$, and the inferred orbital semimajor axis is

$$a = 21.95^{+2.69}_{-2.32}\,R_\odot \simeq 0.1021^{+0.0125}_{-0.0108}\ \text{au}. \tag{19}$$

The corresponding model-inferred total mass is

$$M_{\rm tot} = 1.36^{+0.57}_{-0.39}\,M_\odot, \tag{20}$$

and the component masses are

$$M_1 = 0.93^{+0.39}_{-0.27}\,M_\odot, \qquad M_2 = 0.43^{+0.18}_{-0.12}\,M_\odot, \tag{21}$$

with surface gravities

$$\log g_1 = 4.21^{+0.12}_{-0.11}, \qquad \log g_2 = 2.94^{+0.12}_{-0.12}, \tag{22}$$

in cgs units.

The uncertainties in the masses are substantially larger than those in the fractional light-curve parameters because

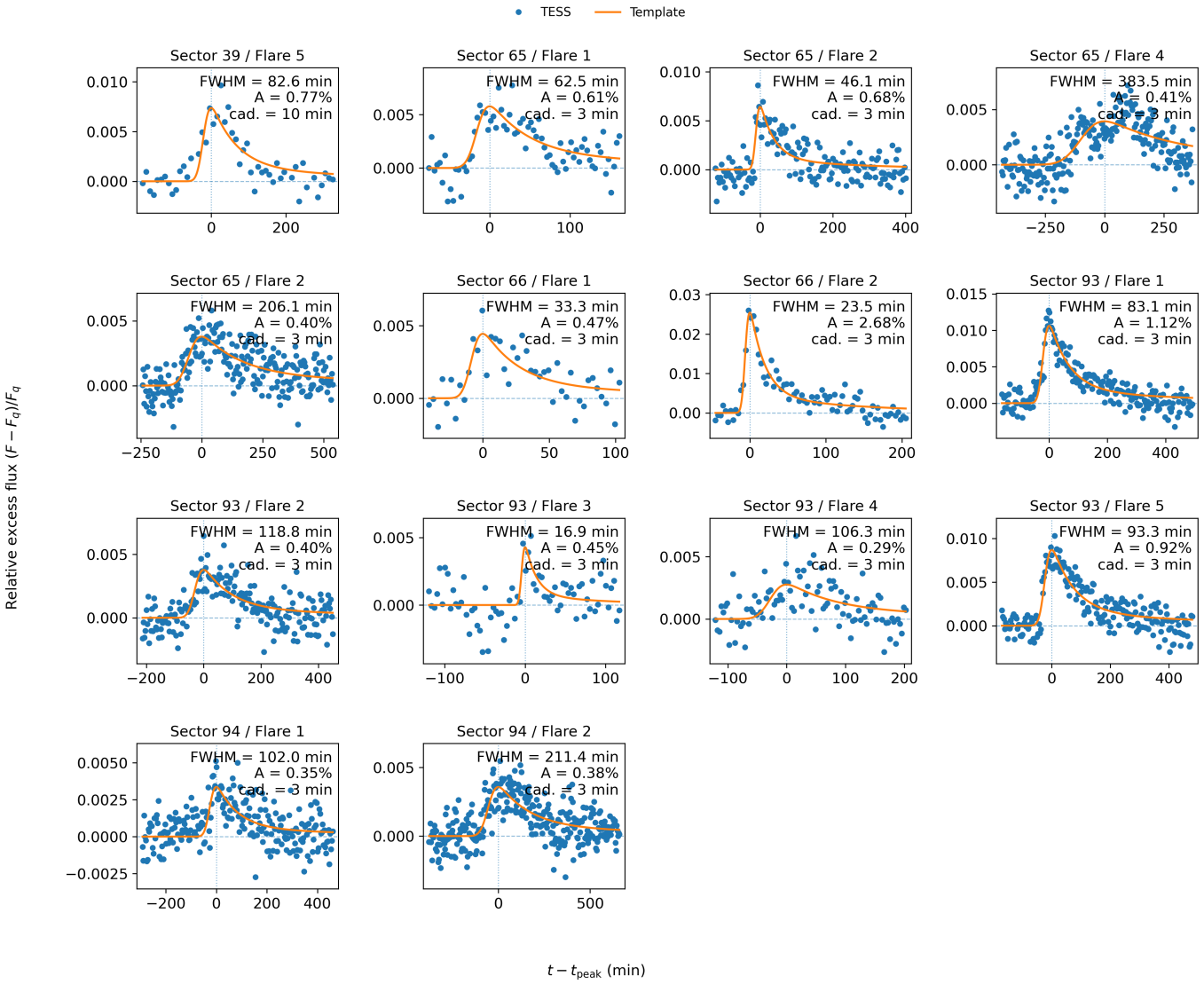


Figure 9. Same as Figure 8, but for the remaining 14 flare candidates identified in the TESS observations of CPD–82 291.

the total mass scales as $M_{tot} \propto a^3$. Consequently, uncertainties or systematic offsets in the SED-derived radius scale are amplified when propagated to the component masses. The mass estimates also depend directly on q_{phot}, which is model dependent in this detached and strongly active system.

The derived radii, masses, and surface gravities are therefore useful for assessing the possible evolutionary state of the components, but they should not be treated as precise mass–radius benchmarks. A double-lined spectroscopic orbit is required to determine the dynamical mass ratio and orbital scale and to test the reliability of the model-inferred absolute parameters. The evolutionary implications of the current solution are considered in Section 4.2.

4.2. Evolutionary Status and Comparison with Similar Systems

The model-inferred stellar parameters derived in Section 4.1 were compared with the pre-main-sequence evolutionary tracks and isochrones of Baraffe et al. (2015) in the T_{eff}–R plane (Figure 10). Because the absolute dimensions of CPD–82 291 are not yet supported by a spectroscopic orbital solution, this comparison is intended to explore possible evolutionary interpretations rather than to establish a unique age or evolutionary state.

The primary component lies close to the zero-age main-sequence region. Within the current uncertainties, its position may be consistent either with a star approaching the main sequence or with one that has already reached the ZAMS. Its

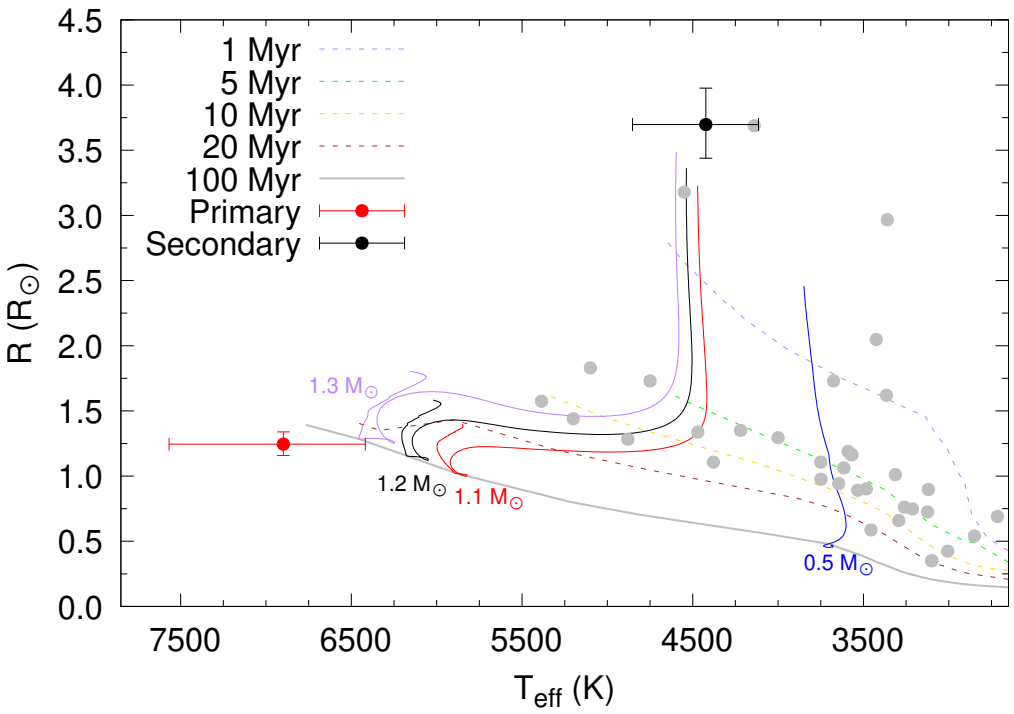


Figure 10. Positions of the components of CPD–82 291 in the $T_{\rm eff}$–R plane, together with the pre-main-sequence evolutionary tracks and isochrones of Baraffe et al. (2015). The primary and secondary components are shown with black and red symbols, respectively. Components of the comparison eclipsing binaries listed in Table 6 are shown as grey circles. The primary lies close to the ZAMS region, whereas the secondary is located well above the main-sequence locus. Because the absolute parameters of CPD–82 291 are model inferred and are not yet supported by a spectroscopic orbit, the diagram illustrates possible evolutionary interpretations rather than establishing a unique pre-main-sequence age or coeval solution.

location therefore does not independently demonstrate a pre-main-sequence evolutionary state.

The secondary component occupies a markedly different region of the diagram. Its comparatively low effective temperature, large inferred radius, and low surface gravity place it well above the main-sequence locus. If the adopted absolute radius scale is approximately correct, this position could be consistent with a low-mass star at an early evolutionary stage. However, the two components do not follow a single well-defined coeval isochrone in the adopted evolutionary models.

Such an apparent discrepancy could be affected by magnetic activity, extensive surface-brightness inhomogeneities, and limitations of standard non-magnetic evolutionary tracks. Starspots may alter the observed effective temperatures and luminosity distribution and can contribute to apparently enlarged radii in active low-mass stars. Nevertheless, activity alone cannot be assumed to explain the position of the secondary. Alternative possibilities include systematic errors in the model-inferred absolute scale, a more evolved secondary, or a previous episode of binary interaction. The available photometry does not distinguish among these interpretations.

This comparison is not methodologically homogeneous. The spectroscopic basis of each literature solution is therefore identified explicitly in Table 6. Most of the comparison systems are double-lined spectroscopic eclipsing binaries (SB 2 EBs), for which both component radial-velocity curves, together with the eclipse light curves, provide dynamical masses. Exceptions are indicated separately in the table; in particular, THOR–42 has a two-component velocity solution in which the secondary velocities were obtained from Hα emission, while MML 48 is a single-lined spectroscopic eclipsing binary whose primary mass was estimated using stellar models. In contrast, no spectroscopic orbit is currently available for CPD–82 291. Its absolute radius scale is inferred from the light-curve and SED solutions using the Gaia distance, and its masses are subsequently estimated from the inferred orbital scale and the photometric mass ratio. The comparison should therefore be regarded as qualitative evolutionary context rather than as a homogeneous dynamical mass–radius benchmark.

The primary component lies within the range occupied by several young eclipsing-binary components of comparable mass and radius. Its properties are compatible with a star approaching the main sequence, but this agreement does not independently establish its youth. The secondary is considerably more unusual. Young systems such as Par 1802, JW 380, and CoRoT 223992193 demonstrate that low-mass pre-main-sequence stars can possess radii substantially larger than their

Table 6
Comparison of the Inferred Parameters of CPD–82 291 with Selected Pre-main-sequence Eclipsing-binary Systems from the Literature

System	P (day)	M_1 ($M_\odot$)	M_2 ($M_\odot$)	R_1 ($R_\odot$)	R_2 ($R_\odot$)	RV basis	References
CPD–82 291	10.205	1.13 ± 0.36	0.53 ± 0.17	1.31 ± 0.08	3.88 ± 0.25	No RV Orbit	This Work
2MASS J05352184-0546085	9.780	0.0572 ± 0.0033	0.0366 ± 0.0022	0.690 ± 0.011	0.540 ± 0.009	SB 2	(1)
JW 380	5.299	0.262 ± 0.025	0.151 ± 0.013	1.189 ± 0.175	0.897 ± 0.170	SB 2	(1,2)
Par 1802	4.674	0.391 ± 0.032	0.385 ± 0.032	1.73 ± 0.02	1.62 ± 0.02	SB 2	(1,2)
CoRoT 223992193	3.875	0.668 ± 0.012	0.4953 ± 0.0073	1.295 ± 0.040	1.107 ± 0.050	SB 2	(1,2)
V1174 Ori	2.635	1.006 ± 0.013	0.7271 ± 0.0096	1.338 ± 0.011	1.063 ± 0.011	SB 2	(1,2)
RX J0529.4+0041A	3.038	1.27 ± 0.01	0.93 ± 0.01	1.44 ± 0.10	1.35 ± 0.10	SB 2	(1,2)
ASAS J0528+03	3.873	1.375 ± 0.028	1.329 ± 0.020	1.83 ± 0.07	1.73 ± 0.07	SB 2	(1,2)
MML 53	2.098	1.0400 ± 0.0067	0.8907 ± 0.0058	1.283 ± 0.043	1.107 ± 0.049	SB 2	(3)
Mon–735	1.975	0.2918 ± 0.0099	0.2661 ± 0.0095	0.762 ± 0.022	0.748 ± 0.023	SB 2	(4)
THOR–42	0.859	0.497 ± 0.005	0.205 ± 0.002	0.659 ± 0.002	0.424 ± 0.002	Two-component RV[†]	(5)
USco 48	2.874	0.738 ± 0.035	0.709 ± 0.035	1.164 ± 0.051	1.164 ± 0.051	SB 2	(6)
TOI–450	10.715	0.1768 ± 0.0004	0.1767 ± 0.0003	0.351 ± 0.003	0.351 ± 0.004	SB 2	(7)
2M1222–57	3.072	0.7354 ± 0.0057	0.6680 ± 0.0044	0.976 ± 0.013	0.942 ± 0.015	SB 2	(8)
2M05–06	1.704	0.424 ± 0.023	0.522 ± 0.028	0.902 ± 0.023	0.891 ± 0.024	SB 2	(9)
2M05–00	1.817	0.348 ± 0.021	0.339 ± 0.019	1.011 ± 0.093	0.725 ± 0.077	SB 2	(9)
MML 48	2.017	1.2 ± 0.07	0.2509 ± 0.0078	1.574 ± 0.054	0.587 ± 0.051	SB 1 + model	(10)

Notes. The "RV basis" column identifies the spectroscopic information entering each solution. "SB 2" denotes a double-lined spectroscopic eclipsing binary for which radial velocities of both eclipsing components are available. For THOR–42 ([†]), the primary velocity was measured from photospheric absorption lines whereas the secondary velocity was obtained from resolved Hα emission. MML 48 is an SB 1 eclipsing binary and its primary mass includes stellar-model information. CPD–82 291 has no spectroscopic orbital solution; its absolute dimensions are model-inferred from the light-curve and SED/Gaia scaling, together with the photometric mass ratio. Accordingly, the systems in this table are shown for qualitative evolutionary comparison and should not be interpreted as a methodologically homogeneous dynamical mass–radius sample.

References: (1) Stassun et al. (2014); (2) Gillen et al. (2017); (3) Gómez Maqueo Chew et al. (2019); (4) Gillen et al. (2020); (5) Murphy et al. (2020); (6) David et al. (2019); (7) Tofflemire et al. (2023); (8) Stassun et al. (2022); (9) Kounkel & Stassun (2024); (10) Chew & Hebb (2025).

main-sequence counterparts. However, the inferred secondary radius of CPD–82 291 is larger than those of most comparison objects, and unlike the literature values, it has not been validated by a dynamical orbital solution.

The strong and changing out-of-eclipse modulation supports the presence of substantial surface activity. Such activity may contribute to the disagreement between the inferred component properties and a single coeval non-magnetic isochrone. However, the displacement of the secondary should not be interpreted uniquely as evidence of pre-main-sequence radius inflation because the absolute scale remains model dependent.

CPD–82 291 also has a relatively long orbital period of $P = 10.20514$ days compared with many known pre-main-sequence eclipsing binaries. If its youth were independently confirmed, it would represent an interesting long-period system for testing early stellar evolution and magnetic activity. At present, however, its Gaia astrometry is inconsistent with physical membership in Chamaeleon I, and no suitable spectroscopy is available to test lithium absorption, Hα emission, surface-gravity indicators, or the systemic radial velocity. CPD–82 291 should therefore not yet be regarded as a secure member of the pre-main-sequence eclipsing-binary population.

4.2.1. Possible Far-infrared Dust Emission

The stellar-only model reproduces the observed SED from the optical region through the WISE W4 band. In particular, the W3 and W4 measurements differ from the stellar-only predictions by only -0.39σ and -0.37σ, respectively. The available optical-to-mid-infrared photometry therefore provides no evidence for a statistically significant infrared excess at wavelengths up to approximately 22 μm.

The only positive long-wavelength deviation is the 60 μm measurement reported by Spangler et al. (2001), $F_{60} = 0.026 \pm 0.019$ Jy, corresponding to a raw significance of only 1.37σ and lying 1.30σ above the stellar-only prediction when the adopted systematic uncertainty is included. This value should therefore not be regarded as a secure far-infrared detection. The corresponding 90 μm result is a non-detection and was incorporated only as a one-sided upper limit. Moreover, the Spitzer/FEPS observations showed no significant excess at 16, 24, or 70 μm. Thus, the possible ISO 60 μm signal has not been independently confirmed by later mid- or far-infrared measurements.

Under the conditional assumption that the low-significance 60 μm emission is physically associated with CPD–82 291, it can be reproduced by a cool circumbinary-dust model. In the

adopted parametrization, the converged MCMC posterior gives characteristic inner and outer radii of $R_{\rm in} = 147^{+37}_{-48}$ au and $R_{\rm out} = 188^{+150}_{-52}$ au. The corresponding dust mass is $(8.1^{+16.0}_{-5.7}) \times 10^{-5}\,M_{\odot}$. This quantity refers specifically to the dust component; no gas-to-dust ratio has been assumed and no total gas+dust disk mass is inferred from the present data. The inferred radii and dust mass are conditional, model-dependent quantities rather than direct measurements of the circumstellar material.

The inferred radial extent and dust mass are strongly model dependent. The disk is spatially unresolved, its inclination was fixed to the binary inclination under an assumed coplanar configuration, and the inferred surface-density normalization depends strongly on the assumed inclination. The outer radius is also poorly constrained by the limited far-infrared information. Consequently, comparisons with resolved disk radii or dynamically characterized Class II disks are not methodologically equivalent, and the fitted mass and radial extent should not be used to classify the system as possessing a typical Class II disk.

The large fitted inner radius should also be considered in relation to the binary orbit. The model-inferred binary semimajor axis is approximately 0.102 au, whereas the conditional disk solution places the inner edge at $R_{\rm in} \simeq 147$ au, giving

$$\frac{R_{\rm in}}{a_{\rm binary}} \simeq 1.4 \times 10^{3}. \tag{23}$$

This scale is far larger than the cavity sizes of a few binary semimajor axes normally associated with tidal truncation by a central binary (Artymowicz & Lubow 1994). We therefore do not interpret the fitted inner radius as evidence for a cavity dynamically cleared by the present binary. Given the weak far-infrared constraint and the model dependence of the inferred disk parameters, the present data cannot establish the physical origin of such a large characteristic inner radius.

The radial-emission diagnostics shown in Figure A4 illustrate the temperature profile and wavelength-dependent emitting regions predicted by the conditional disk model. They are entirely model derived and do not represent spatially resolved observations. In particular, they should not be used as independent evidence for the inferred disk geometry or radial extent.

The spectral index measured between 2 and 24 μm is $\alpha = -2.68 \pm 0.05$. According to the classification boundaries adopted by Großschedl et al. (2019), this value lies in the Class III/no-IR-excess regime. In the present case, however, the evolutionary status of the source is not independently established and the WISE and Spitzer photometry is consistent with photospheric emission. We therefore use α only as a descriptive measure of the optical-to-mid-infrared SED slope. It supports the absence of a strong warm inner-disk contribution but does not establish the presence of an evolved circumbinary disk.

Taken together, the available observations do not securely demonstrate that CPD–82 291 hosts a gravitationally bound circumbinary disk. The adopted cool-dust model provides one possible representation of the tentative far-infrared signal if that signal is physically associated with the binary. Confirmation requires new far-infrared or millimetre observations with substantially improved sensitivity and angular resolution.

4.3. Surface and Flare Activity

The sector-specific models show that the out-of-eclipse modulation cannot be represented by a single static surface-brightness configuration. Broad cool regions assigned to the secondary provide an effective description of the dominant modulation, while different cool and hot regions are required on the primary at different epochs. This supports the general conclusion that CPD–82 291 exhibits substantial surface activity.

The fitted parameters are generally more similar in temporally adjacent sectors than between epochs separated by several years, which is consistent with short-term persistence and longer-term changes in the overall activity pattern. However, the large fitted angular radii of approximately 65°–82° should not be interpreted as the sizes of single physical spots. Their fitted dimensions and positions are degenerate with the adopted temperature contrast, viewing geometry, luminosity ratio, and number of surface-brightness regions, and may represent combinations of multiple unresolved active structures.

Likewise, changes in the fitted longitudes do not demonstrate the migration of the same physical spot, and the fitted colatitudes near 90° do not establish an equatorial concentration of activity. The robust result is therefore the changing large-scale surface-brightness distribution rather than the detailed geometry, latitude, lifetime, or migration of individual fitted regions.

The changing surface-brightness distribution inferred from the light-curve modelling is accompanied by recurrent flare activity in the TESS photometry. A total of 28 flare events were retained in the final sample. Because the temporal sampling differs substantially among the observed sectors, ranging from approximately 30–3.33 minutes, the flare timescales were interpreted with explicit reference to the cadence of the corresponding data. One event in Sector 11 was detected above the adopted threshold in only a single cadence and therefore did not provide a resolved threshold-defined duration or FWHM. Consequently, the duration and FWHM statistics below refer to the remaining 27 temporally resolved events, whereas the amplitude and equivalent-duration statistics include all 28 flares.

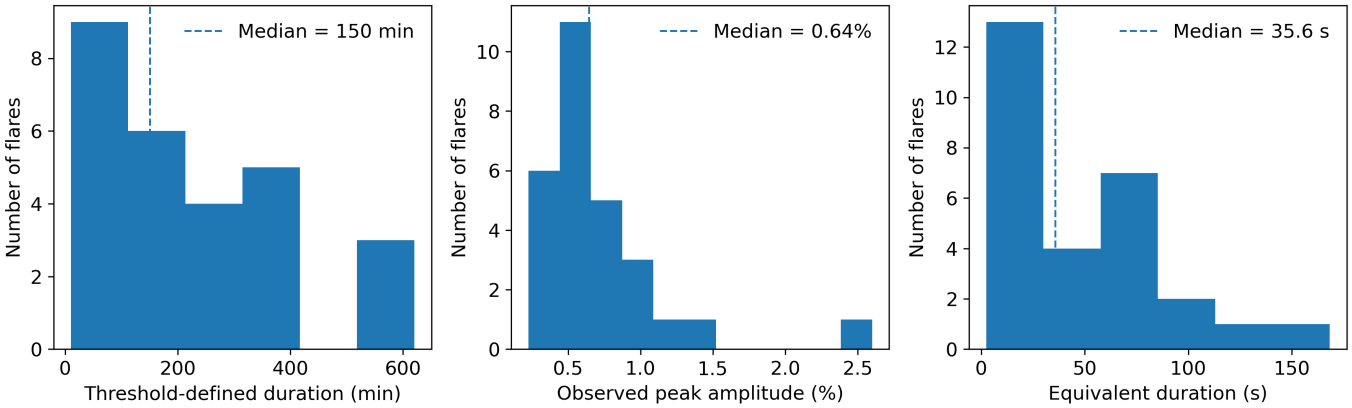


Figure 11. Statistical properties of the 28 flare events retained in the final sample. Left: distribution of the threshold-defined durations for the 27 events with resolved start and end times. Middle: distribution of the observed peak amplitudes for all 28 events. Right: distribution of the directly integrated equivalent durations. Dashed vertical lines indicate the corresponding median values.

The threshold-defined durations span approximately 10–620 minutes, with a median of 150.0 minutes and a mean of 218.6 minutes. The corresponding analytic-template FWHM values range from 16.9 to 383.5 minutes, with a median of 81.9 minutes and a mean of 95.0 minutes. These quantities should not be interpreted as exact intrinsic flare timescales, particularly for events sampled at the longer TESS cadences, but they provide a consistent characterization of the observed flare profiles across the available sectors.

The observed peak amplitudes are generally modest. The median relative flux enhancement is 0.643%, while the largest event reaches 2.60%. The directly integrated equivalent durations range from 2.39 to 168.37 s, with a median of 35.65 s and a mean of 47.92 s. The distributions of threshold-defined duration, observed peak amplitude, and directly integrated equivalent duration are shown in Figure 11.

Within the detected flare sample, the equivalent duration is positively correlated with both the observed flare timescale and the peak amplitude (see Figure 12). For the directly integrated equivalent duration and threshold-defined duration, the Spearman rank coefficient is $\rho_S = 0.718$ with a 95% bootstrap confidence interval of [0.433, 0.865] ($p = 2.5 \times 10^{-5}$; $N = 27$). A similar correlation is obtained between equivalent duration and the template FWHM, with $\rho_S = 0.689$ and a 95% confidence interval of [0.410, 0.871] ($p = 7.0 \times 10^{-5}$; $N = 27$). The correlation between equivalent duration and observed peak amplitude is comparably strong (see Figure 12), $\rho_S = 0.720$, with a 95% confidence interval of [0.450, 0.854] ($p = 1.5 \times 10^{-5}$; $N = 28$). In contrast, the relation between peak amplitude and threshold-defined duration is weaker and is not statistically significant (see Figure 12), with $\rho_S = 0.322$ and a 95% confidence interval of [−0.089, 0.634] ($p = 0.101$; $N = 27$). Thus, the present sample does not indicate that event duration is the dominant factor associated with flare equivalent duration; instead, both flare amplitude and temporal extent show comparably strong correlations with the observed equivalent duration. These relations are descriptive of the detected events and should not be interpreted as completeness-corrected population relations.

The equivalent durations obtained from the analytic flare templates closely track those measured directly from the detrended data. The two quantities show a very strong rank correlation ($\rho_S = 0.976$, $p = 7.6 \times 10^{-19}$), demonstrating that the adopted analytic profiles reproduce the overall flare-strength ordering of the sample. The template-derived equivalent durations are nevertheless systematically larger, with a median ratio $ED_{\rm model}/ED_{\rm data} = 1.44$. This difference is expected because the analytic profiles include extended decay tails beyond the portion of the event directly sampled within the manually selected integration interval. For this reason, the directly integrated equivalent duration is adopted as the primary observational measure in the statistical analysis, while the template-derived value is retained as a model-dependent diagnostic.

The number of identified events varies among the individual TESS sectors, from two to six flares per sector. These raw counts should not, however, be interpreted directly as changes in the intrinsic flare rate. The sectors differ both in temporal sampling and in usable observing duration, and the detectability of low-amplitude or short-duration events is correspondingly cadence dependent. A quantitative comparison of flare occurrence rates between sectors would therefore require an explicit completeness analysis and normalization by the effective observing time. We accordingly restrict the present discussion to the properties of the detected flare sample rather than interpreting the sector-to-sector counts as evidence for long-term changes in the magnetic activity level.

Taken together, the evolving large-scale surface-brightness distribution and the recurrent flare detections establish CPD–82 291 as an active eclipsing system. However, neither the

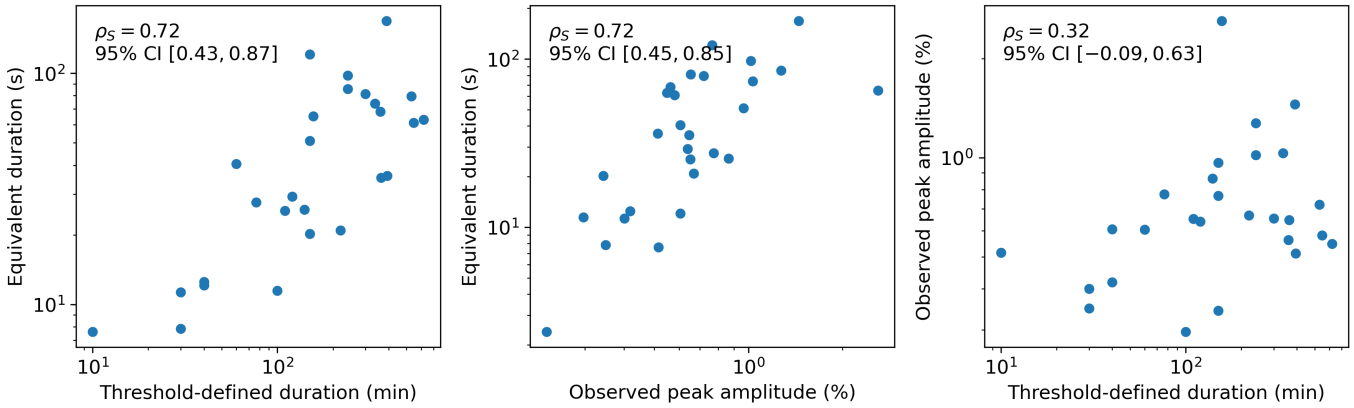


Figure 12. Relations among the measured flare properties. Left: directly integrated equivalent duration versus threshold-defined duration. Middle: equivalent duration versus observed peak amplitude. Right: observed peak amplitude versus threshold-defined duration. The Spearman rank coefficient, ρ_S, is indicated in each panel.

parametrized surface-brightness regions nor the flare measurements uniquely identify the active component, the physical sizes of individual magnetic structures, or the presence of persistent active longitudes or magnetic cycles. The robust observational result is therefore the coexistence of evolving photospheric modulation and recurrent flare activity over multiple TESS observing epochs.

4.4. Model Limitations and Future Observational Tests

The posterior distributions of the SED parameters reveal significant degeneracies within the adopted model. The strongest correlations are found between the stellar effective temperature and stellar radius ($r = -0.82$), and between the stellar effective temperature and reddening ($r = +0.93$). Such behaviour is expected in broadband SED modelling because an increase in effective temperature can be partly compensated by either a smaller stellar radius or a larger reddening, producing a similar optical continuum shape. A weaker anti-correlation is present between the outer disk radius and the surface-density normalization ($r = -0.39$), reflecting the partial degeneracy between the radial extent and dust content of the conditional disk model.

The stellar parameters are better constrained than the circumstellar parameters because the optical-to-mid-infrared photometry provides substantially greater leverage on the stellar contribution, while the light-curve ratios and Gaia distance further reduce the allowed stellar parameter space. Significant covariance nevertheless remains, particularly among $T_{\star,1}$, $R_{\star,1}$, and $E(B-V)$. The stellar parameters obtained from the converged SED posterior, $T_{\star,1} = 6898^{+670}_{-480}$ K and $R_{\star,1} = 1.245^{+0.094}_{-0.087}\,R_\odot$, are consistent with the observed multi-wavelength photometry under the adopted light-curve constraints on the temperature and radius ratios. As an external comparison, the StarHorse estimate (Anders et al. 2022) gives $A_V = 0.55^{+0.01}_{-0.07}$ mag [$E(B-V) = 0.177^{+0.004}_{-0.024}$ for $R_V = 3.1$], which is consistent, within the broad posterior uncertainties, with our SED result of $E(B-V) = 0.130^{+0.110}_{-0.089}$. We use the StarHorse estimate only as an external consistency check and do not interpret the comparison as evidence for local or circumbinary extinction.

The circumstellar parameters are substantially more weakly constrained than the stellar parameters, with broad and asymmetric posterior distributions. In particular, the outer radius is $R_{\rm out} = 188^{+150}_{-52}$ au for the present conditional model. This weak constraint results from the very limited far-infrared information, which consists of a low-significance 60 μm measurement and a 90 μm upper limit. The photometry through the WISE W4 band is consistent with the stellar photospheres alone. Consequently, the circumstellar posterior quantifies the range of parameters permitted under the conditional assumption that the tentative far-infrared signal is physically associated with the system, rather than demonstrating that such a component is required by the data. The inferred surface density, dust mass, and disk radii remain model dependent and also depend on the assumed inclination, opacity law, temperature prescription, and radial density profile.

A further major limitation is the absence of a spectroscopic orbital solution. The light-curve analysis constrains the fractional radii, orbital inclination, temperature ratio, and a model-dependent photometric mass ratio, while the primary radius is inferred from the SED using the Gaia distance and the secondary radius follows from the light-curve radius ratio. The orbital scale is then obtained from the combination of the SED-based radius and the corresponding fractional radius. Consequently, the component masses, absolute radii, and orbital scale are model inferred rather than dynamically determined. Double-lined radial-velocity observations covering the orbit are required to determine the dynamical mass

ratio and orbital scale and to test the reliability of the model-inferred absolute parameters.

The evolutionary status of CPD–82 291 also remains uncertain. Its Gaia astrometry is incompatible with physical membership in Chamaeleon I, and no suitable spectra are presently available from which lithium absorption, Hα emission, surface-gravity indicators, or a systemic radial velocity can be measured. The PMS interpretation must therefore remain tentative. Spectroscopy covering the Li I 6708 Å line, Hα, and suitable photospheric absorption lines would provide direct tests of its youth, activity, and orbital properties.

The sector-by-sector light-curve solutions demonstrate a changing large-scale surface-brightness distribution, but the fitted circular regions are non-unique representations of the observed asymmetries. Their sizes, temperature contrasts, and locations are mutually degenerate and should not be interpreted as uniquely reconstructed physical spots. Multi-band photometry and time-resolved spectroscopy would help separate temperature-contrast effects from geometric surface-brightness variations.

Finally, confirmation of the possible far-infrared dust component requires new observations at far-infrared or millimetre wavelengths with substantially improved sensitivity and angular resolution. Such observations would determine whether the tentative long-wavelength emission is associated with CPD–82 291 and would provide meaningful constraints on the temperature, mass, and radial extent of any surrounding material.

5. Conclusions

In this study, we present a multi-sector TESS photometric and spectral energy distribution analysis of the eclipsing binary CPD–82 291. Although the system has historically been classified as a young star in the direction of Chamaeleon I, the Gaia DR3 astrometry rules out physical membership in that association, and no spectroscopic youth diagnostics or radial-velocity orbit are currently available. The evolutionary status of the system therefore remains uncertain. Our main results can be summarized as follows:

1. The multi-sector TESS light curves show pronounced out-of-eclipse variability whose morphology changes between observing epochs. Sector-by-sector surface-brightness modelling requires different configurations at different epochs, supporting evolving large-scale photospheric inhomogeneities. The fitted regions should, however, be regarded as non-unique parametrizations of the surface-brightness distribution rather than literal maps of individual starspots. The configurations are generally more similar in temporally adjacent sectors, but the changing sizes and longitudes do not uniquely establish long-lived individual spots, spot migration, active longitudes, or magnetic cycles.
2. A total of 28 flare events were retained in the final TESS sample. Their observed peak amplitudes have a median value of 0.64%, while the directly integrated equivalent durations have a median of 35.6 s. For the 27 events with resolved threshold-defined durations, the median duration is approximately 150 minutes. Equivalent duration is significantly correlated with both flare timescale and peak amplitude, whereas the correlation between peak amplitude and duration is weak and not statistically significant. The flare detections, together with the evolving photospheric modulation, establish CPD–82 291 as an active eclipsing system.
3. The reference light-curve solution is consistent with a detached binary viewed at an orbital inclination of $i \simeq 82.^{\circ}1$. The photometric modelling yields $q_{\rm phot} \simeq 0.464$; in the absence of a spectroscopic orbit, this mass ratio is model dependent and should not be interpreted as a dynamical measurement.
4. The stellar photospheric model reproduces the observed SED through the WISE W4 band without requiring an infrared-excess component. The reported 60 μm flux is only a low-significance measurement (0.026 ± 0.019 Jy), while the 90 μm result is a non-detection and is included only as a one-sided upper limit. Consequently, the available photometry does not provide secure evidence for a bound circumbinary dust disk.
5. Under the conditional assumption that the marginal far-infrared signal is physically associated with the system, a cool-dust model can reproduce it, with posterior median radii of $R_{\rm in} \simeq 147$ au and $R_{\rm out} \simeq 188$ au. These quantities are strongly model dependent and non-unique. The inferred inner radius is approximately 1.4×10^3 times the model-inferred binary separation and therefore should not be interpreted as a conventional tidally truncated circumbinary cavity.
6. In the absence of radial velocities, the absolute scale is model-inferred by combining the SED-derived primary radius at the adopted Gaia distance with the fractional light-curve parameters. The current solution gives approximately $R_1 \simeq 1.25\,R_\odot$, $R_2 \simeq 3.70\,R_\odot$, $M_1 \simeq 0.93\,M_\odot$, and $M_2 \simeq 0.43\,M_\odot$. These values are not dynamical measurements, and the mass uncertainties are amplified by the cubic dependence of the total mass on the inferred orbital scale, while the absolute radii depend on the SED-derived radius scale and light-curve radius ratio.
7. Comparison with stellar evolutionary calculations places the primary close to the ZAMS, whereas the secondary lies substantially above the main-sequence locus if the inferred absolute scale is correct. The two components

do not define an unambiguous coeval PMS solution. The secondary's position may reflect activity-related structural effects, limitations of the inferred absolute scale, or limitations of the evolutionary models; it cannot by itself be taken as evidence for youth or PMS radius inflation.

8. CPD–82 291 should therefore presently be regarded as an active eclipsing binary of uncertain evolutionary status, with marginal far-infrared emission but no secure evidence for a circumbinary disk. Time-series double-lined spectroscopy is the most important next step, as it would provide the dynamical orbital scale and component masses, systemic velocity, and independent atmospheric and youth diagnostics. More sensitive far-infrared or millimetre observations with improved angular resolution are likewise required to determine whether any cold circumstellar or circumbinary material is physically associated with the system.

Acknowledgments

We thank the anonymous referee for their insightful and constructive suggestions that significantly improved the paper. This study forms part of the preliminary work associated with TÜBİTAK project proposal No. 126F230. We gratefully acknowledge TÜBİTAK.

The numerical calculations reported in this paper were partially performed at the TÜBİTAK ULAKBİM High Performance and Grid Computing Center (TRUBA resources).

We acknowledge the use of TESS High Level Science Products (HLSP) produced by the Quick-Look Pipeline (QLP) at the TESS Science Office at MIT, which are publicly available from the Mikulski Archive for Space Telescopes (MAST). Funding for the TESS mission is provided by NASA's Science Mission directorate. The data described here may be obtained from the MAST archive via Huang et al. (2020). This research made use of Lightkurve, a Python package for Kepler and TESS data analysis (Lightkurve Collaboration et al. 2018).

This work has made use of data from the European Space Agency (ESA) mission Gaia (https://www.cosmos.esa.int/gaia), processed by the Gaia Data Processing and Analysis Consortium (DPAC).

This research has made use of the SIMBAD database and the VizieR catalog access tool, operated at CDS, Strasbourg, France.

This publication makes use of data products from the Wide-field Infrared Survey Explorer (WISE), which is a joint project of the University of California, Los Angeles, and the Jet Propulsion Laboratory/California Institute of Technology, funded by NASA.

Facilities: HST (STIS), Swift (XRT and UVOT), AAVSO, CTIO:1.3m, CTIO:1.5m, CXO.

Software: `PHOEBE` (Prša & Zwitter 2005; Prša et al. 2016; Horvat et al. 2018; Conroy et al. 2020; Jones et al. 2020), `Astropy` (Astropy Collaboration et al. 2013, 2018, 2022), `corner` (Foreman-Mackey 2016), `Lightkurve`(Lightkurve Collaboration et al. 2018), `Matplotlib` (Hunter 2007), `NumPy` (C. R. Harris et al. 2020).

Author Contributions

All editors contribute equally to the operation of PASP.

Appendix
Additional MCMC and Model Figures

This appendix presents the posterior probability distributions obtained from the MCMC analyses performed for both the light-curve (Figures A1–A3) and SED modelling (Figures A4–A6). The corner plots provide a visual representation of the parameter uncertainties, correlations, and possible degeneracies within the adopted models. Median parameter values and confidence intervals reported in the main text were derived from these posterior distributions.

A.1. Light-Curve MCMC and Surface Geometry

This subsection presents additional figures related to the light-curve modelling of CPD–82 291. The appendix includes the corner plot obtained from the MCMC analysis (Figure A3) and the component surface mesh plots (Figures A1–A2) corresponding to the adopted binary configuration.

The corner plot illustrates the posterior distributions and parameter correlations derived from the MCMC analysis of the light-curve solution. The distributions indicate that the principal orbital and stellar parameters are generally well constrained by the high-precision TESS photometry, although moderate correlations remain between inclination, surface potentials, temperature ratios, and spot-related parameters.

The component surface mesh plots provide a model-based visualization of the Roche geometry and adopted surface-brightness distributions of the binary components, including the spot configurations used to reproduce the observed out-of-eclipse asymmetries. These surface representations should not be interpreted as unique maps of individual starspots.

A.2. Supplementary SED Model Diagnostics

This appendix presents supplementary diagnostics associated with the conditional circumstellar-dust interpretation discussed in Section 3.3. These figures are provided to illustrate the behaviour and parameter degeneracies of the adopted model and should not be interpreted as independent evidence for the presence of a bound circumbinary disk. The corresponding model diagnostics and alternative photospheric comparison are shown in Figures A4 and A5, respectively.

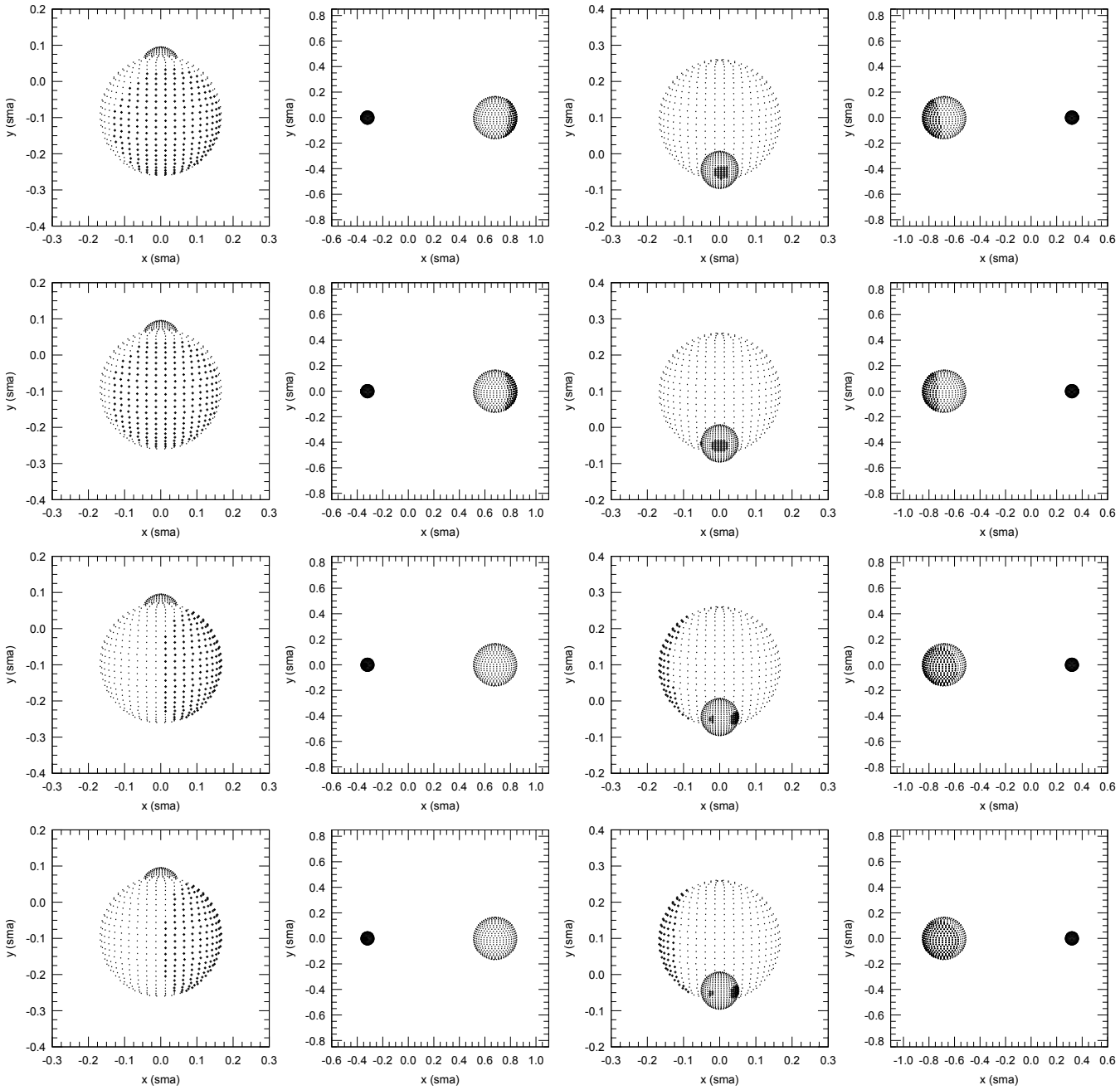


Figure A1. Surface mesh representations of the binary components at four different orbital phases, from left to right, 0, 0.25, 0.50, and 0.75, respectively, for the light-curve solutions obtained from TESS Sectors 11, 13, 38, and 39 (from top to bottom, respectively). The models illustrate the evolution of the spot configurations and the corresponding changes in the longitudinal distribution of the active regions between different observing epochs. The adopted spot parameters are listed in Table 5.

The corner plot below shows the posterior distributions obtained when the circumstellar-dust component is retained as a conditional part of the SED model. Strong correlations are present among extinction, stellar temperature, and stellar radius, as expected from broadband SED fitting. The circumstellar parameters are more weakly constrained, with broad and asymmetric posterior distributions reflecting the very limited far-infrared information available for this system. In particular, the low-significance 60 μm measurement and the 90 μm upper limit do not uniquely constrain the radial structure or dust mass of the conditional model. The light-curve constraints on the stellar temperature and radius ratios, together with the Gaia distance,

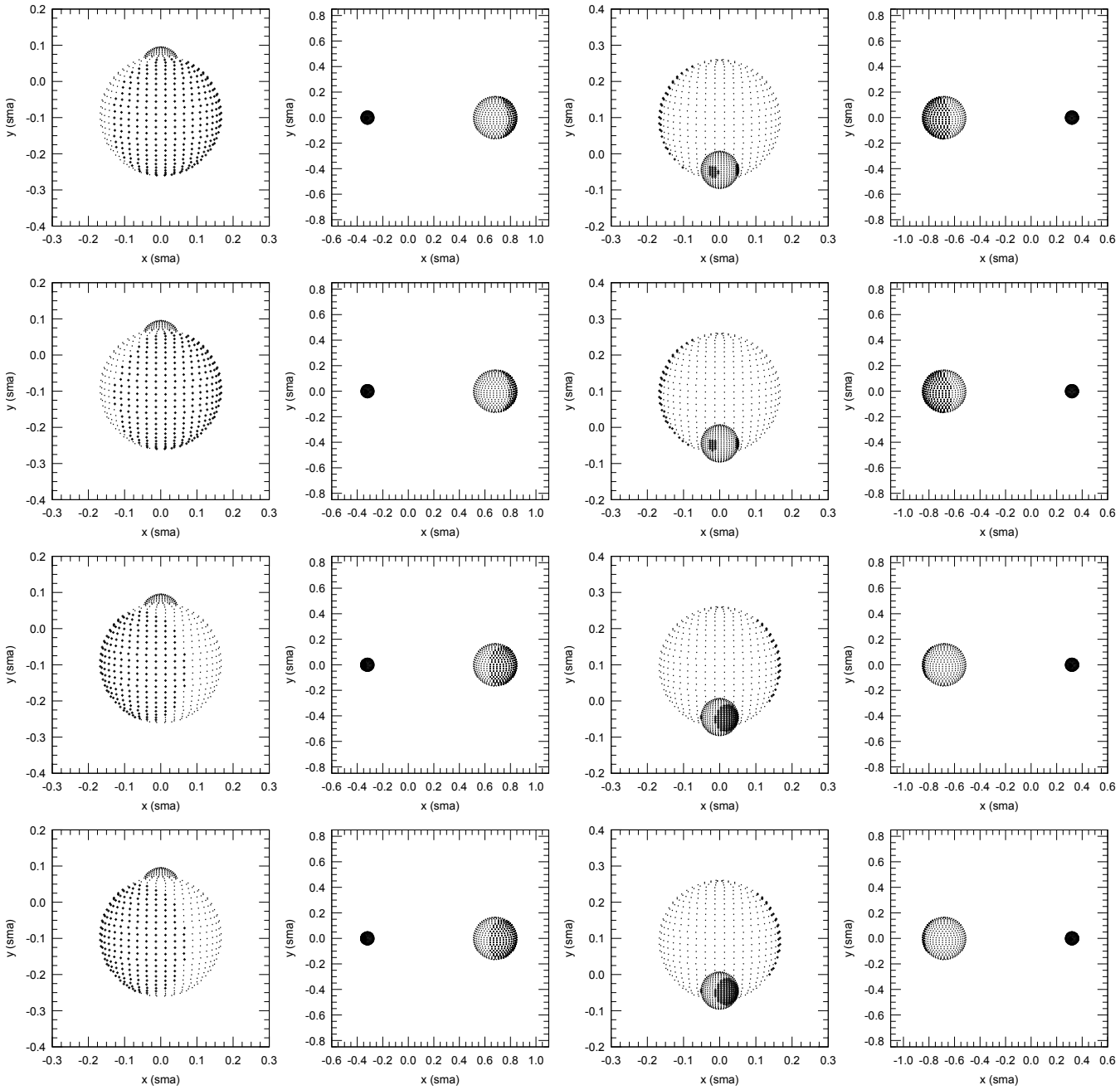


Figure A2. Same as Figure A1, but for TESS Sectors 65, 66, 93, and 94 (from top to bottom, respectively).

reduce the freedom in the stellar component of the model, but they do not remove the substantial uncertainties in the circumstellar parameters. Consequently, these posterior distributions should be interpreted as parameter constraints conditional on the adopted dust model rather than as evidence that such a component is required by the data. The corresponding posterior distributions and parameter covariances are shown in Figure A6.

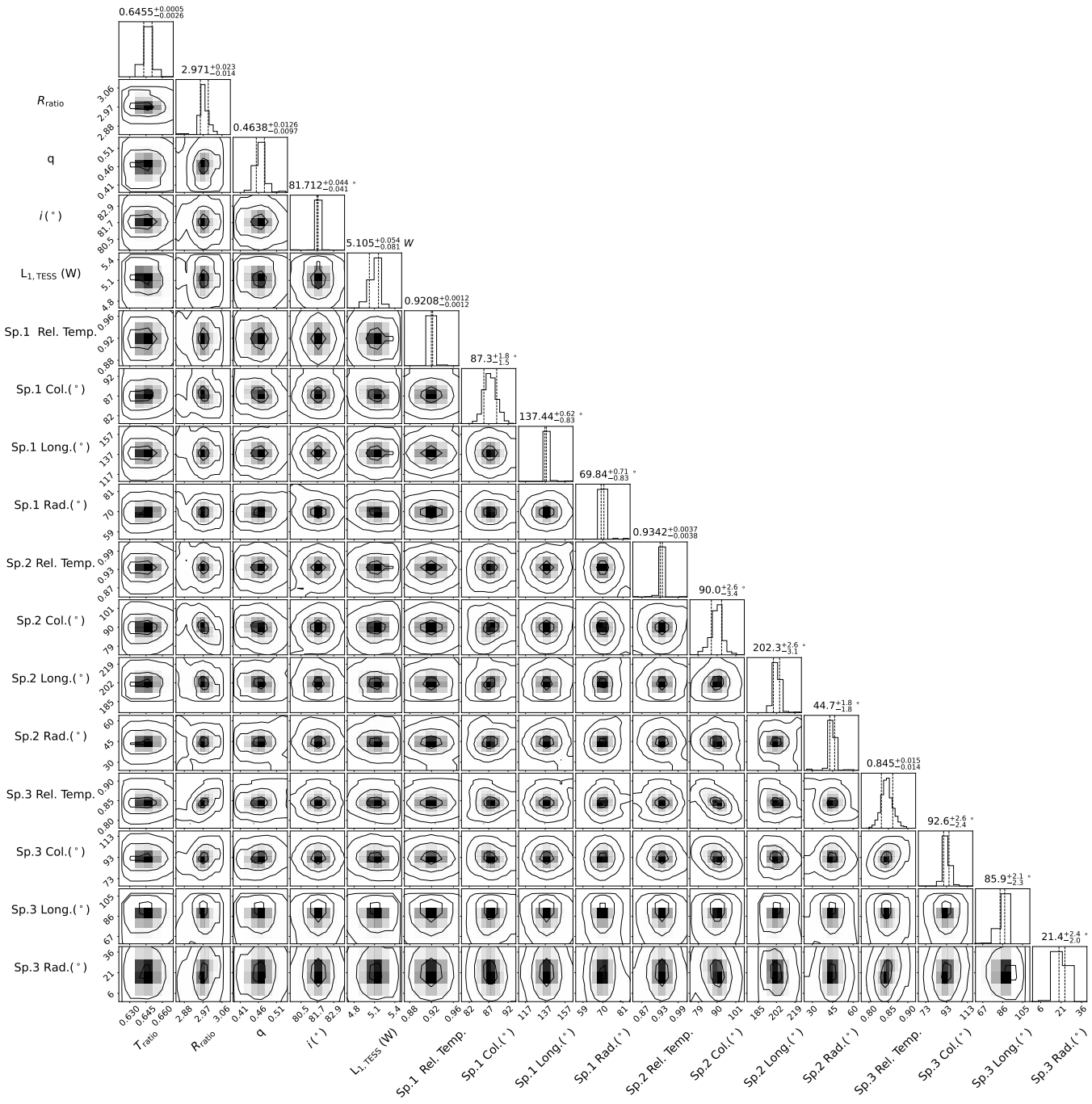


Figure A3. Posterior distributions and parameter correlations for the light curve model obtained from the MCMC analysis. The diagonal panels show the marginalized distributions, while the off-diagonal panels illustrate parameter covariances. Contours indicate the highest posterior density regions at 68%, 95%, and 99.7%.

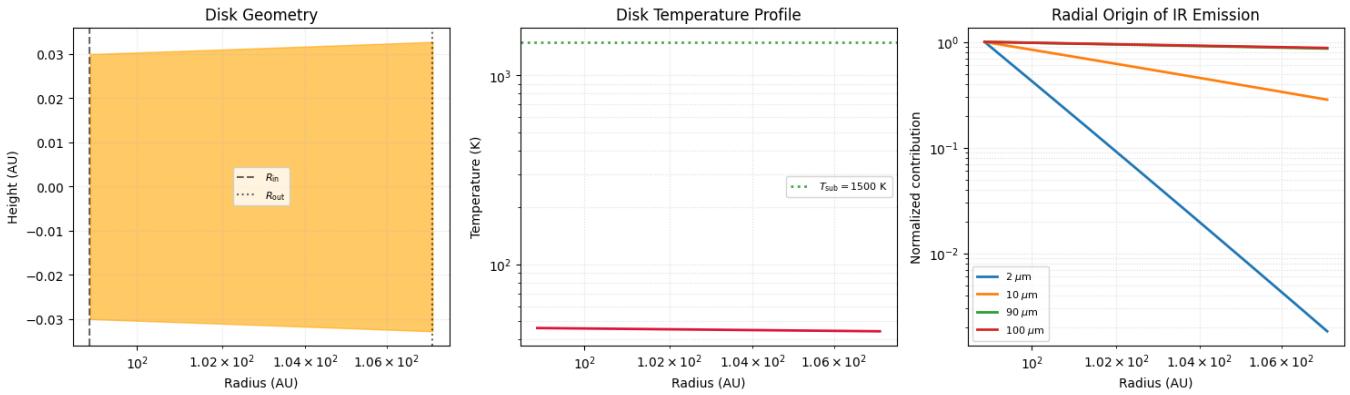


Figure A4. Disk-structure diagnostics for the adopted conditional circumstellar-dust model. Left: Model representation of the radial–vertical geometry of the parametrized flared disk. Middle: Temperature profile of the passively irradiated disk, following a power-law decrease with radius; the horizontal line indicates the approximate dust sublimation temperature. Right: Predicted radial contribution to the thermal emission at representative wavelengths within the adopted model, illustrating that progressively longer wavelengths are predicted to receive relatively greater contributions from cooler material at larger radii. These diagnostics are entirely model-derived and do not constitute spatially resolved measurements or a unique reconstruction of the circumstellar structure.

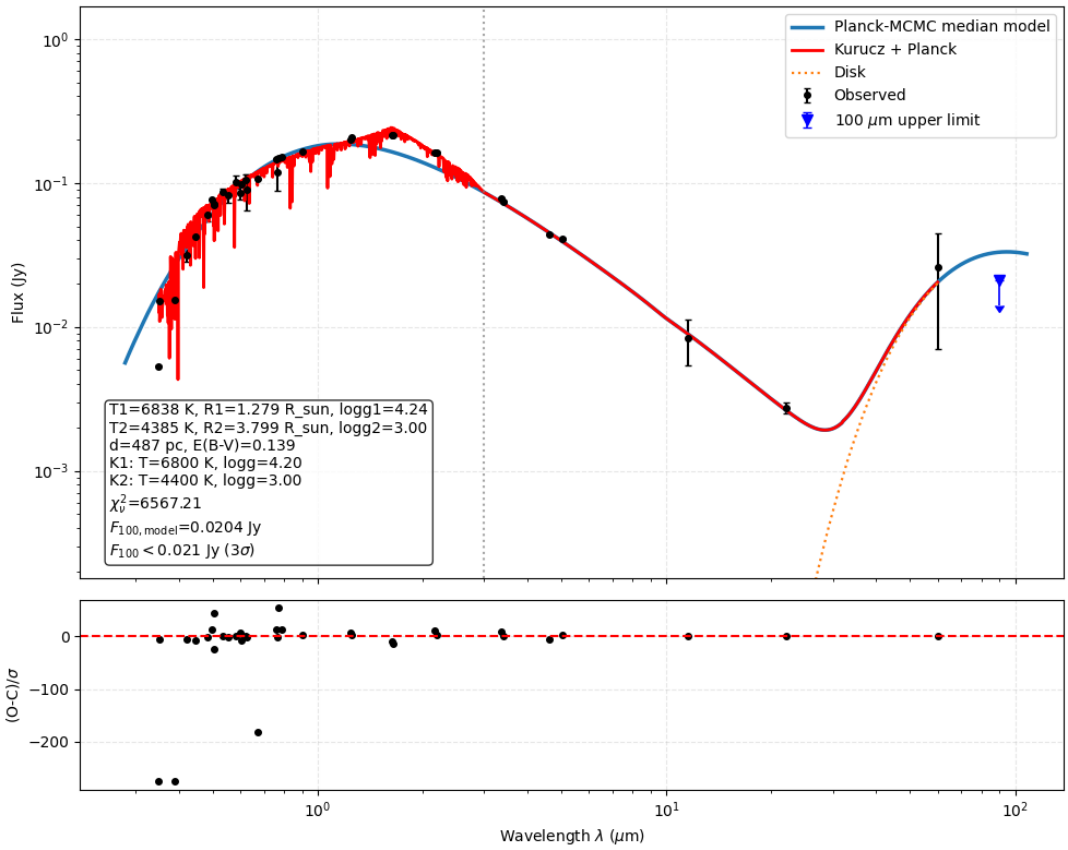


Figure A5. Supplementary comparison of the observed SED with alternative representations of the stellar photospheres. Top panel: Black circles show the observed fluxes. The solid red curve corresponds to the hybrid model constructed using Kurucz stellar atmospheres combined with the conditional circumstellar-dust component, while the black curve shows the median blackbody-based MCMC model. The dotted line represents the dust contribution within the conditional model. The 90 μm upper limit is indicated by a blue downward arrow, whereas the low-significance 60 μm measurement provides the only positive far-infrared deviation from the stellar photospheres. The vertical dotted line marks the wavelength at which the dust contribution becomes dominant in the conditional model and should not be interpreted as an observationally determined transition wavelength. Bottom panel: Normalized residuals $(O - C)/\sigma$ for the hybrid model. The Kurucz-atmosphere calculation is included only as a supplementary consistency check and was not used to derive the SED posterior parameters quoted in the main analysis. Both photospheric representations support the conclusion that no significant infrared excess is required through the WISE W4 band.

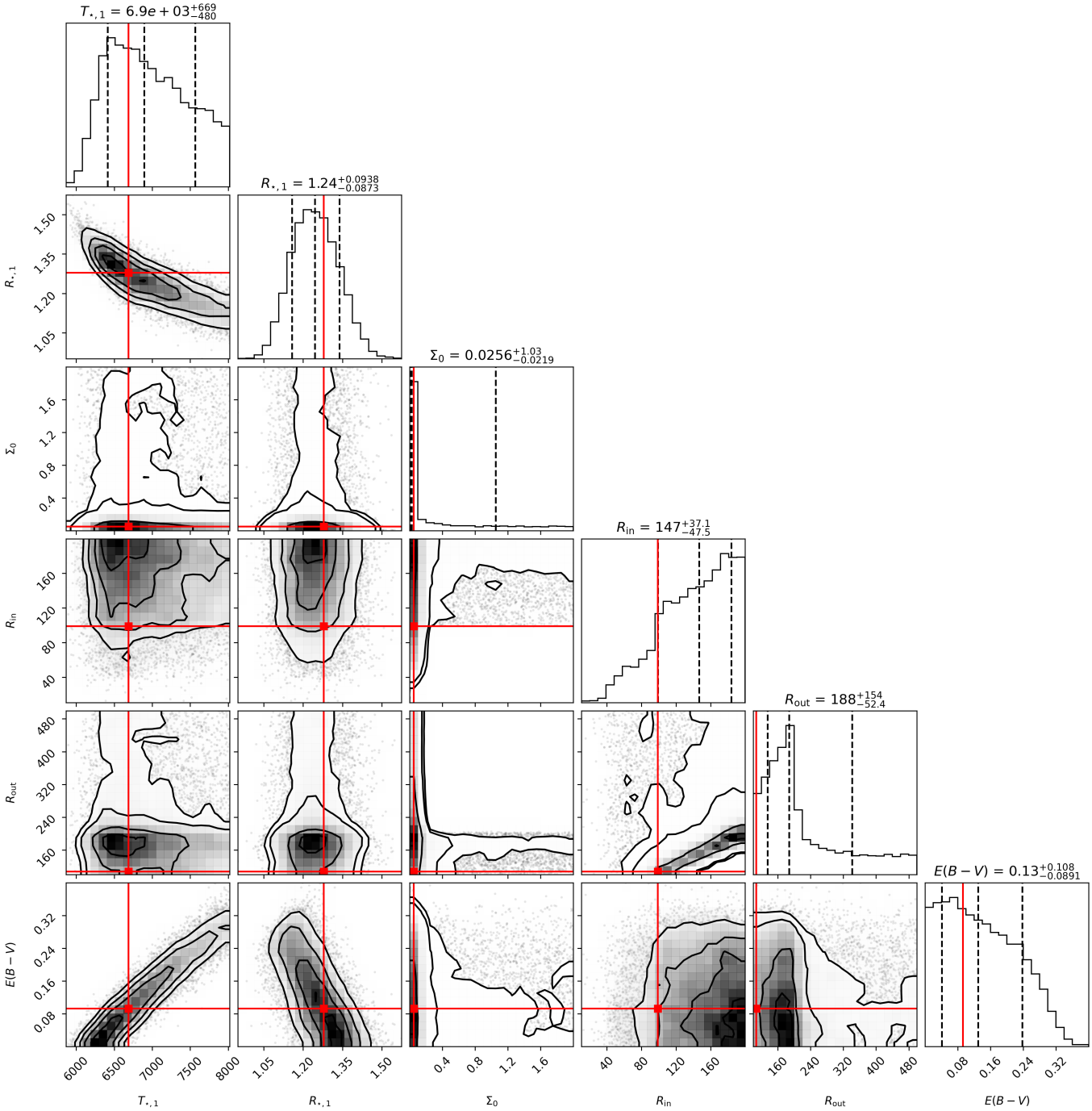


Figure A6. Posterior distributions and parameter correlations for the conditional circumstellar-dust SED model obtained from the MCMC analysis. The diagonal panels show the marginalized distributions, while the off-diagonal panels illustrate parameter covariances. Contours indicate the highest posterior density regions at 68%, 95%, and 99.7%. The broad and correlated circumstellar posteriors reflect the weak far-infrared constraints and should not be interpreted as a unique determination of the disk properties.

ORCID iDs

Volkan Bakış https://orcid.org/0000-0002-3125-9010
Gökhan Yücel https://orcid.org/0000-0002-9846-3788

References

Anders, F., Khalatyan, A., Queiroz, A. B. A., et al. 2022, A&A, 658, A91
Artymowicz, P., & Lubow, S. H. 1994, ApJ, 421, 651
Astropy Collaboration, Price-Whelan, A. M., Lim, P. L., et al. 2022, ApJ, 935, 167
Astropy Collaboration, Price-Whelan, A. M., Sipőcz, B. M., et al. 2018, AJ, 156, 123
Astropy Collaboration, Robitaille, T. P., Tollerud, E. J., et al. 2013, A&A, 558, A33
Bakış, I., & Habalı, A. Y. 2026, PARep, 4, 29
Baraffe, I., Homeier, D., Allard, F., & Chabrier, G. 2015, A&A, 577, A42
Carpenter, J. M., Bouwman, J., Mamajek, E. E., et al. 2009, ApJS, 181, 197
Chew, Y. G. M., & Hebb, L. 2025, A&A, 702, 17
Christy, C. T., Jayasinghe, T., Stanek, K. Z., et al. 2022, PASP, 134, 024201
Conroy, K. E., Kochoska, A., Hey, D., et al. 2020, ApJS, 250, 34
David, T. J., Hillenbrand, L. A., Gillen, E., et al. 2019, ApJ, 872, 161
Foreman-Mackey, D. 2016, JOSS, 1, 24
Foreman-Mackey, D., Hogg, D. W., Lang, D., & Goodman, J. 2013, PASP, 125, 306
Gillen, E., Hillenbrand, L. A., David, T. J., et al. 2017, ApJ, 849, 11
Gillen, E., Hillenbrand, L. A., Stauffer, J., et al. 2020, MNRAS, 495, 1531
Gómez Maqueo Chew, Y., Hebb, L., Stempels, H. C., et al. 2019, A&A, 623, A23
Gordon, K. D., Clayton, G. C., Decleir, M., et al. 2023, ApJ, 950, 86
Großschedl, J. E., Alves, J., Teixeira, P. S., et al. 2019, A&A, 622, A149
Harris, C. R., Millman, K. J., van der Walt, S. J., et al. 2020, Natur, 585, 357
Horvat, M., Conroy, K. E., Pablo, H., et al. 2018, ApJS, 237, 26
Huang, C. X., Vanderburg, A., Pál, A., et al. 2020, RNAAS, 4, 204
Hunter, J. D. 2007, CSE, 9, 90
Jayasinghe, T., Stanek, K. Z., Kochanek, C. S., et al. 2019, MNRAS, 485, 961
Jones, D., Conroy, K. E., Horvat, M., et al. 2020, ApJS, 247, 63
Kounkel, M., & Stassun, K. G. 2024, AJ, 168, 134
Kwee, K. K., & van Woerden, H. 1956, BAN, 12, 327
Lemke, D., Klaas, U., Abolins, J., et al. 1996, A&A, 315, L64
Lightkurve Collaboration, Cardoso, J. V. d. M., Hedges, C., et al. 2018, Lightkurve: Kepler and TESS time series analysis in Python, ascl:1812.013
Murphy, S. J., Lawson, W. A., Onken, C. A., et al. 2020, MNRAS, 491, 4902
Ochsenbein, F., Bauer, P., & Marcout, J. 2000, A&AS, 143, 23
Prša, A., & Zwitter, T. 2005, ApJ, 628, 426
Prša, A., Conroy, K. E., Horvat, M., et al. 2016, ApJS, 227, 29
Roccatagliata, V., Sacco, G. G., Franciosini, E., & Randich, S. 2018, A&A, 617, L4
Serenelli, A., Weiss, A., Aerts, C., et al. 2021, A&ARev, 29, 4
Shappee, B., Prieto, J., Stanek, K. Z., et al. 2014, AAS Meeting, 223, 236.03
Spangler, C., Sargent, A. I., Silverstone, M. D., Becklin, E. E., & Zuckerman, B. 2001, ApJ, 555, 932
Stassun, K. G., Feiden, G. A., & Torres, G. 2014, NewAR, 60, 1
Stassun, K. G., Torres, G., Kounkel, M., et al. 2022, ApJ, 941, 125
Tofflemire, B. M., Kraus, A. L., Mann, A. W., et al. 2023, AJ, 165, 46
Torres, G., Andersen, J., & Giménez, A. 2010, A&ARev, 18, 67
Tovar Mendoza, G., Davenport, J. R. A., Agol, E., Jackman, J. A. G., & Hafwley, S. L. 2022, AJ, 164, 17